Paramagnetic NMR Shifts of *Tris*-Hypersilanide Early f-Block Metal(III) Complexes

Benjamin L. L. Réant,[1] Fraser J. Mackintosh,[1] Gemma K. Gransbury,[1] Carlo Andrea Mattei,[1] Barak Alnami,[1] Benjamin Atkinson,[1] David Bonham,[2] Jack Baldwin,[1] Ashley J. Wooles,[1] Iñigo J. Vitorica-Yrezabal,[1] Daniel Lee,[2,*] Nicholas F. Chilton,[1,3,*] Stephen T. Liddle,[1,*] and David P. Mills[1,*]

[1]*Department of Chemistry, The University of Manchester, Oxford Road, Manchester, M13 9PL, U.K.*

[2]*Department of Chemical Engineering, The University of Manchester, Oxford Road, Manchester, M13 9PL, U.K.*

[3]*Research School of Chemistry, The Australian National University, Sullivans Creek Road, Canberra, 2601, ACT, Australia.*

**Email: daniel.lee@manchester.ac.uk; nicholas.chilton@anu.edu.au; steve.liddle@manchester.ac.uk; david.mills@manchester.ac.uk.*

Abstract

The paramagnetism of f-block ions has been exploited in chiral shift reagents and magnetic resonance imaging, but these applications tend to focus on ^{1}H NMR shifts as paramagnetic broadening makes less sensitive nuclei more difficult to study. Here we report a solution and solid-state (ss) ^{29}Si NMR study of an isostructural series of locally D_{3h}-symmetric early f-block metal(III) *tris*-hypersilanide complexes, [M{Si(SiMe$_3$)$_3$}$_3$(THF)$_2$] (**1-M**; M = La, Ce, Pr, Nd, U); **1-M** were also characterized by single crystal and powder X-ray diffraction, EPR, ATR-IR and UV-Vis-NIR spectroscopies, SQUID magnetometry and elemental analysis. Only one SiMe$_3$ signal was observed in the ^{29}Si ssNMR spectra of **1-M**, whilst two SiMe$_3$ signals were seen in solution ^{29}Si NMR spectra of **1-La** and **1-Ce**. This is attributed to dynamic averaging of the SiMe$_3$ groups in **1-M** in the solid state due to free rotation of the M–Si bonds, and dissociation of THF from **1-M** in solution to give the locally C_{3v}-symmetric complexes [M{Si(SiMe$_3$)$_3$}$_3$(THF)$_n$] (n = 0 or 1), which show restricted rotation of M–Si bonds on the NMR timescale. Density functional theory and complete active space self-consistent field spin-orbit calculations were performed on **1-M** and desolvated solution species to model paramagnetic NMR shifts. We find excellent agreement of experimental ^{29}Si NMR data for diamagnetic **1-La**, suggesting n = 1 in solution, and reasonable agreement of calculated paramagnetic shifts of SiMe$_3$ groups for **1-M** (M = Pr and Nd); the NMR shifts for metal-bound ^{29}Si nuclei could only be reproduced for diamagnetic **1-La**, showing the current limitations of pNMR calculations for larger nuclei.

Introduction

f-Block metal complexes have been exploited in a wide range of applications that take advantage of their remarkable magnetic and optical behaviour,[1] including chiral shift reagents[2-4] and PARASHIFT tags for Magnetic Resonance Imaging (MRI),[5-7] emissive probes for microscopy[8-10] and biomolecules,[11-16] and in determining spin-spin coupling in multi-metallic systems.[17-19] Nuclear Magnetic Resonance (NMR) spectroscopy is widely used to study these parameters and is also a useful technique to assess purity, to investigate exchange coupling and dynamic processes, and to extract kinetic and thermodynamic parameters.[20] As the vast majority of f-block ions are paramagnetic,[1] the nuclear hyperfine interaction with unpaired electrons in valence f-orbitals give NMR spectra with significant paramagnetic shifts and line broadening.[21-23] Whilst the ^{1}H NMR spectra of paramagnetic f-block complexes can often be assigned and correlated with calculated values to benchmark electronic structures,[21] less receptive heteroatomic nuclei often give intractable spectra, thus systematic investigations are rare.[24]

Molecular lanthanide (Ln) and actinide (An) alkyl chemistry is well-developed, with numerous examples of homoleptic Ln(III) *tris*-alkyl complexes.[25,26] Conversely, f-block silanide chemistry is relatively immature and Ln(III) *tris*-silanide complexes are unknown to date.[27] More broadly, the applications of f-block silicon chemistry include σ-bond metathesis reactions promoted by Ln silanide complexes,[28,29] the addition of Ln silicides to low-alloy steels,[30] and the use of An silicides as high density nuclear fuels.[31-34] Most structurally authenticated f-block silanide complexes contain the hypersilanide ligand, {Si(SiMe$_3$)$_3$}, or related derivatives;[27,35] selected examples include [Ln{Si(SiMe$_3$)$_3$}$_2$(THF)$_3$] (Ln = Sm, Eu, Yb),[36] [Yb(C$_5$Me$_5$){Si(SiMe$_3$)$_3$}(THF)$_2$],[37] [Y{Si(SiMe$_3$)$_3$}(I)$_2$(THF)$_3$],[38] [Sc(Cp)$_2$\{Si(SiMe$_3$)$_3$\}(THF)] (Cp = C$_5$H$_5$),[39] [K(18-crown-6)][Ln(Cp)$_3$\{Si(SiMe$_3$)$_3$\}] (Ln = Ho, Tm; Cp = cyclopentadienyl),[40] [{K(18-crown-6)}$_2$Cp][Ln(Cp)$_3$\{Si(SiMe$_3$)$_3$\}] (Ln = Ce, Sm, Gd, Tm),[40] [M(Cp″)$_2$\{Si(SiMe$_3$)$_3$\}] (M = La, Ce, Nd, U; Cp″ = {C$_5$H$_3$(SiMe$_3$)$_2$-1,3}),[41] [Y{C(PPh$_2$SiMe$_3$)$_2$}\{Si(SiMe$_3$)$_3$\}(THF)],[42] [U{N(ᵗBu)(C$_6$H$_3$Me$_2$-3,5)}\{Si(SiMe$_3$)$_3$\}],[43] [U(C$_5$H$_4$SiMe$_3$)$_3$\{Si(SiMe$_3$)$_3$\}],[44] and [K(sol1)][U{[Si(SiMe$_3$)$_2$SiMe$_2$]$_2$O}(sol2)(I)$_2$] (sol1 = (DME)$_4$, sol2 = DME; sol1 = 18-crown-6, sol2 = DME or (THF)$_2$).[45] Recently, we used a combination of ^{29}Si NMR spectroscopy and density functional theory (DFT) calculations to quantify covalency in diamagnetic *n*f^{14} M(II)–Si bonds for M = Yb and No.[46] However, these methods are not simply transferable to paramagnetic f-block complexes, where a fully *ab initio* approach needs to be employed to sufficiently account for open-shell effects in paramagnetic NMR (pNMR) spectra.[47]

Here we report a solution and solid-state (ss) ^{29}Si NMR study of an isostructural series of trigonal bipyramidal early f-block metal(III) *tris*-hypersilanide complexes, [M{Si(SiMe$_3$)$_3$}$_3$(THF)$_2$] (**1-M**; M = La, Ce, Pr, Nd, U); **1-M** are

also characterized by single crystal and powder X-ray diffraction, EPR, ATR-IR and UV-Vis-NIR spectroscopies, SQUID magnetometry, elemental analysis, and DFT and complete active space self-consistent field spin-orbit (CASSCF-SO) calculations. We find that **1-M** each have only one $SiMe_3$ resonance in their ^{29}Si ssNMR spectra, which we attribute to dynamic averaging of the $SiMe_3$ groups due to free rotation of the M–Si bonds, whilst dissociation of THF in solution gives the trigonal pyramidal species $[M\{Si(SiMe_3)_3\}_3(THF)_n]$ (n = 0 or 1), which typically exhibit two $SiMe_3$ signals in their ^{29}Si NMR spectra due to restricted rotation of the M–Si bonds on the NMR timescale. We find excellent agreement of experimental ^{29}Si NMR data with DFT-calculated values for diamagnetic **1-La**, and reasonable agreement with CASSCF-SO-calculated paramagnetic shifts of $SiMe_3$ groups for **1-M** (M = Pr and Nd); the NMR shifts for metal-bound ^{29}Si nuclei could only be reproduced for diamagnetic **1-La**, showing the current limitations of predictive pNMR calculations for larger nuclei where significant contact shifts are implicated.

Results

Synthesis. Complexes **1-M** were prepared by salt metathesis reactions between solvated trivalent metal iodide precursors, $[MI_3(THF)_x]$ (M = La, Ce, Pr, U, x = 4; M = Nd, x = 3.5), and three equivalents of potassium hypersilanide, $[K\{Si(SiMe_3)_3\}]$, in diethyl ether (Scheme 1). Crystalline samples of **1-M** were obtained in *ca.* 40% yields (range = 33-51%) following work-up and recrystallisation from hexane. Microcrystalline **1-M** showed nearly superimposable ATR-IR spectra (see Supporting Information Figures S42-S47), indicating that they have similar solid-state structures. We consistently obtained low carbon values for **1-M** in elemental analyses; we attribute this to incomplete combustion due to silicon carbide formation as this has been postulated for f-block silicon complexes previously, and we note that elemental analysis experiments can be capricious.[48,49] We therefore interrogated **1-M** by powder XRD, and found high phase purity in all cases (see Supporting Information Figures S57-S67 and Table S2).

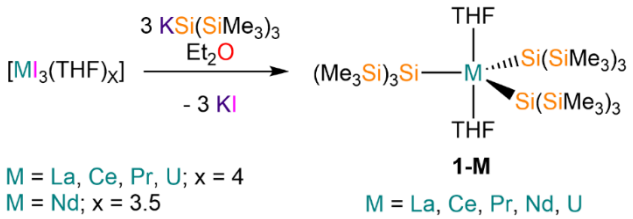

Scheme 1. Synthesis of **1-M**.

Structural Characterization. The molecular structures of **1-M** were confirmed by single crystal XRD (**1-U** is shown in Figure 1 and key metrical parameters for all **1-M** are compiled in Table 1; see Supporting Information Figures S53-S56

for depictions of other **1-M** and Table S3 for additional crystallographic data). Complexes **1-M** exhibit trigonal bipyramidal geometries, with three hypersilanide ligands in the equatorial plane and two axially-bound THF molecules. All structures show 120° Si–M–Si angles, with only slight deviations of O–M–Si and O–M–O angles from their respective ideal values (90° and 180°) for local D_{3h} point symmetry arising from modelling coordinated THF about a three-fold rotation axis; **1-Pr** shows a larger deviation from D_{3h} in the solid state as it crystallizes in $P6_3$, in contrast with the $P6_3/m$ space group of other **1-M**. The relative distortions of **1-M** were quantified by calculating τ_5 parameters, which show the degree of trigonality in a five-coordinate complex ($\tau_5 = (\beta - \alpha)/60$; β is the largest and α the second-largest angle in the coordination sphere); $\tau_5 = 1$ is ideal trigonal bipyramidal and $\tau_5 = 0$ is a square based pyramid.[50] For most of the **1-M** series $\tau_5 = 1$, whereas for **1-Pr** $\tau_5 = 0.98$.

As expected M–Si and M–O distances decrease across the Ln series with Ln(III) cation size,[51] with the M–Si distance in $5f^3$ **1-U** (3.114(2) Å) shorter than the corresponding distance in $4f^3$ **1-Nd** (3.131(2) Å) but longer than the sum of covalent radii of U and Si (2.86 Å).[52] Complex **1-Pr** contains the first structurally authenticated example of a Pr–Si bond, whilst the M–Si distances of **1-La**, **1-Ce**, **1-Nd** and **1-U** are comparable with previously reported hypersilanide complexes of these respective M(III) ions,[27] e.g. $[M(Cp'')_2\{Si(SiMe_3)_3\}]$ (M = La, 3.178(2) Å; Ce, 3.153(2) Å; Nd, 3.112(2) Å; U, 3.116(2) Å)[41] and $[\{K(18\text{-crown-6})\}_2Cp]][Ce(Cp)_3\{Si(SiMe_3)_3\}]$ (3.155(2) Å).[40] Structurally authenticated U–Si bonds are rare,[27] but have recently been expanded to include the family of U(III) complexes $[K(sol1)][U\{[Si(SiMe_3)_2SiMe_2]_2O\}(sol2)(I)_2]$ (sol1 = $(DME)_4$, sol2 = DME; sol1 = 18-crown-6, sol2 = DME or $(THF)_2$) (range U–Si: 3.1149(6)–3.1713(14) Å).[45] In all solid-state structures of **1-M** three Si–Si bonds are located in the plane defined by the central MSi_3 motifs, and the remaining six Si–Si bonds are equally arranged above and below this plane in a fan arrangement.

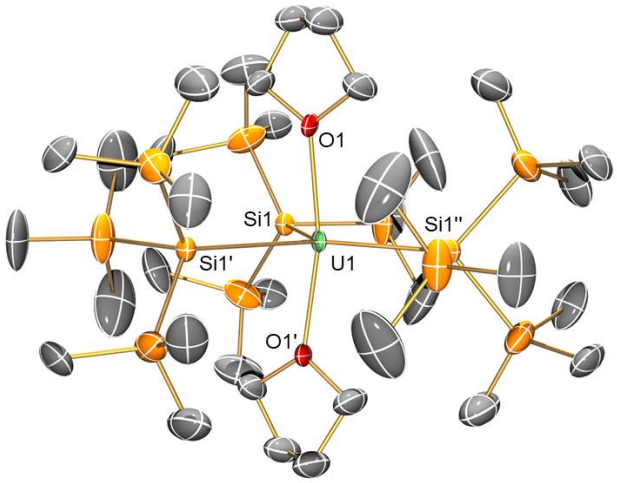

Figure 1. Molecular structure of **1-U** with selective atom labelling collected at 150 K. Displacement ellipsoids set at 30% probability level and hydrogen atoms removed for clarity.

Table 1. M–Si and M–O bond distances (Å) and angles (°) for **1-M**.

	1-La	**1-Ce**	**1-Pr**	**1-Nd**	**1-U**
M–Si/ Å	3.197(3)	3.172(2)	3.161(3)	3.131(2)	3.114(2)
M–O/ Å	2.461(11)	2.389(10)	2.36(2), 2.51(2)	2.407(6)	2.442(6)
Si–M–Si / °	120	120	120	120	120
O–M–Si / °	90.03(11)	90.14(7)	87.6(2), 91.3(2)	90.0(4)	90.03(5)
O–M–O / °	180	180	178.8(2)	180	180

Solution NMR Spectroscopy. Despite the paramagnetism of **1-Ce**, **1-Pr**, **1-Nd** and **1-U**, we were able to assign solution ^{1}H, ^{13}C{^{1}H} and ^{29}Si DEPT90 NMR spectra for all complexes (see Supporting Information Figures S1-S28 for all solution NMR spectra and Table S1 for selected parameters; selected data are compiled in Table 2); these assignments were verified by ^{1}H COSY, ^{1}H–^{13}C HMBC and HSQC, and ^{1}H–^{29}Si HMBC experiments. Although ^{1}H→^{29}Si polarization transfer using the DEPT90 approach is expected to increase the sensitivity of ^{29}Si signals, we note that it is not optimal for concomitant ^{2}J and ^{3}J scalar coupling so the metal-bound Si resonances have low intensities. However, during previous investigations of paramagnetic metal complexes using ^{29}Si NMR spectroscopy we have consistently found that signals are most frequently observed in DEPT90 experiments.[41,44,46] C_6D_6 solutions of **1-M** fully decomposed within 10 minutes to $HSi(SiMe_3)_3$ (assigned by comparison with an authentic sample; (δ_{Si} in C_6D_6 = –11.6 ppm, $SiMe_3$; –115.6 ppm, HSi)[53]) and other products. Resonances associated with a potential impurity, $[K\{Si(SiMe_3)_3\}]$ (δ_{Si} in THF = –4.55 ppm, $SiMe_3$; –194.10 ppm, KSi),[54] were not observed. NMR data were therefore acquired on *ca.* 9 : 1 C_6D_6 : C_4D_8O solutions of **1-M** (50 mM) that have decomposition $t_{1/2}$ > 2 hrs, allowing reliable ^{1}H NMR integrals to be extracted. We

found that C_4D_8O had to be added before C_6D_6 to obtain acceptable NMR spectra, which still contained signals consistent with $HSi(SiMe_3)_3$ and silicone grease impurities; other decomposition products that reproducibly formed were not identified (Solutions of **1-Pr** showed the fastest decomposition, see Supporting Information Section 1.6. and Figures S29-S31 for a systematic study).

A sample of **1-La** with an internal standard of 1,3,5-tri-*tert*-butylbenzene was dissolved in neat C_4D_8O in an effort to reduce sample decomposition prior to collection of NMR spectra and to investigate THF exchange dynamics further. However, this did not provide NMR data that were easier to interpret than those obtained for the 9 : 1 C_6D_6 : C_4D_8O solution due to the complex exchange behavior, thus we did not extend this study to C_4D_8O solutions of paramagnetic **1-M** (see Supporting Information Section 1.7. and Figures S32-S34 for an extended discussion). The ^1H and $^{13}C\{^1H\}$ NMR spectra of **1-La**, **1-Ce** and **1-U** exhibit only slightly shifted THF resonances compared to free THF; the THF signals in the ^1H NMR spectra are broadened with non-reliable integrals, and THF resonances are not assigned in samples of **1-Pr** and **1-Nd**. We note that a number of signals are observed in the ^1H and $^{13}C\{^1H\}$ NMR spectra of **1-Pr** and **1-Nd** that may arise from THF, but we do not assign them as their identity is uncertain due to sample decomposition and complex exchange equilibria. The lower gyromagnetic ratio of ^{13}C nuclei in combination with the generally short relaxation times in these samples precluded the assignment of THF signals *via* correlation experiments.

Together, these data indicate that THF may dissociate from **1-M** in solution to give $[M\{Si(SiMe_3)_3\}_3(THF)_n]$ (n = 0 or 1), which hereafter we respectively refer to as $M(THF)_0$ and $M(THF)_1$. We posit that the loss of coordinated THF and generation of vacant coordination site(s) is the origin of the relatively facile solution decomposition of **1-M**, as previously found for $[Ln(Si^tBu_2R)_2(THF)_3]$ (Ln = Sm, Eu, Yb, R = Me; Ln = Sm, Eu, R = ^{t}Bu).[46] The ^1H NMR spectra of **1-M** each contain two resonances for the $SiMe_3$ groups in a 1 : 2 ratio (herein referred to as group 1 and group 2, respectively), confirming that the time-averaged structures are still three-fold symmetric; we note that the resonances associated with group 2 are broad (FWHM > 65 Hz) for the most paramagnetic M(III) ions in **1-Nd** and **1-U**.

Table 2. Selected ^{1}H, ^{29}Si DEPT90 and ^{13}C{^{1}H} NMR chemical shifts (ppm) for **1-M**.

Complex	^{1}H NMR			^{29}Si DEPT90 NMR		^{13}C{^{1}H} NMR
	δ_H(Si(CH_3)$_3$) Group 1	δ_H(Si(CH_3)$_3$) Group 2	$\Delta(\delta_H)$	δ_{Si}(M*Si*)	δ_{Si}(*Si*Me$_3$)	δ_C(Si(*C*H$_3$)$_3$)
1-La	0.23	0.41	0.18	–82.3	–13.1 (Group 1), –5.3 (Group 2)	1.39 (Group 1), 6.78 (Group 2)
1-Ce	1.55	–1.43	2.98	–79.4	–11.4 (Group 1), –6.4 (Group 2)	2.78 (Group 1), 6.30 (Group 2)
1-Pr	8.13	–7.66	15.79	–65.5	–2.9 (Group 1)	9.74 (Group 1)
1-Nd	5.08	–4.63	9.71	–71.6	–6.8 (Group 1)	6.51 (Group 1)
1-U	5.63	–6.84	12.47	–70.5	–6.0 (Group 1)	7.05 (Group 1)

Whilst two resonances were seen for SiMe$_3$ groups in both the ^{13}C{^{1}H} and ^{29}Si DEPT90 NMR spectra of **1-La** and **1-Ce**, only resonances associated with group 1 were observed in the corresponding spectra of **1-Pr**, **1-Nd** and **1-U**; this is likely due to the increased anisotropic paramagnetic broadening associated with these ions.[1] Resonances between δ_{Si} values of –65.5 and –82.3 ppm in the ^{29}Si DEPT90 NMR spectra of **1-M** were assigned to the metal-bound silicon atoms (Figure 2); the ^{29}Si DEPT NMR spectral windows were +175 to –225 ppm. The ^{29}Si shifts observed fall within a relatively narrow range, considering the differences in both paramagnetism and size of the metal ions across the **1-M** series, as the exchange dynamics will vary with metal-ligand distances. The consistent observation of metal-bound silicon resonances for the most paramagnetic **1-M** when some SiMe$_3$ resonances were not seen is in accord with increased line-broadening for the latter signals from dynamic THF exchange outweighing the relative effects of paramagnetic broadening. In the ^{1}H–^{29}Si HMBC NMR spectra of **1-M** correlations were seen between δ_{Si}(M*Si*) and the δ_H(Si(CH_3)$_3$) signals corresponding to group 1, but no cross-peaks were observed between δ_{Si}(M*Si*) and the group 2 SiMe$_3$ groups. For **1-La** and **1-Ce** cross-peaks were seen between δ_H(Si(CH_3)$_3$) and δ_{Si}(Si(CH_3)$_3$) for both the group 1 and group 2 SiMe$_3$ groups, whereas for **1-Pr**, **1-Nd** and **1-U** correlations were only observed for the group 1 SiMe$_3$ groups, as the group 2 SiMe$_3$ resonances were not observed by ^{13}C{^{1}H} and ^{29}Si DEPT90 NMR spectroscopy (see above).

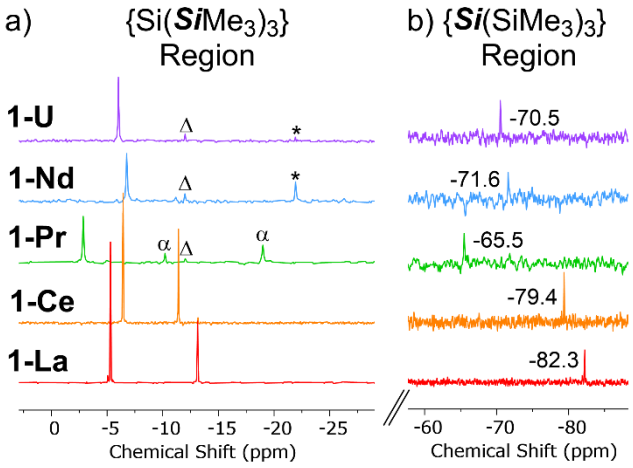

Figure 2. Stacked truncated ^{29}Si DEPT90 NMR spectra (79.48 MHz) of **1-M** in 9 : 1 C_6D_6 : C_4D_8O showing a) *Si*Me_3 resonances between 0 and –25 ppm and b) M*Si* resonances between –60 and –85 ppm. α = unidentifiable species, Δ = $HSi(SiMe_3)_3$ impurity, * = silicone grease impurity.

Solid-State NMR Spectroscopy. As solution NMR spectroscopy indicated that THF readily dissociates from **1-M** in solution to give $[M\{Si(SiMe_3)_3\}_3(THF)_n]$ (n = 0 or 1), we turned to ssNMR spectroscopy to characterize trigonal bipyramidal **1-M** with a known geometry (see Table 3 and Supporting Information Table S2 for selected parameters, Figure 3 for the ^{29}Si ssNMR spectra, and Supporting Information Figures S35-S41 for all other spectra). Magic angle spinning (MAS) conditions were employed with spinning frequencies between 5 and 12 kHz; frequencies were selected depending on the sample to give adequate resolution and signal-to-noise ratios, while shifting the spinning side bands from the spectral regions of interest and limiting excessive spinning rates to avoid rotor crashes. The resolution (FWHM) of the ^{29}Si ssNMR resonances did not change with MAS frequency (slow (5 kHz) *vs*. moderate (12 kHz) spinning), but the ^{1}H ssNMR spectral resolution varied dramatically as expected (see Supporting Information).

For diamagnetic **1-La**, the signal in the ^{29}Si MAS NMR spectrum at δ_{iso} = –102.6 ppm is assigned to the metal-bound Si atoms (Figure 3). The lineshape of this signal is consistent with an eight-line multiplet owing to the J coupling to ^{139}La (I = 7/2, 99.9% naturally abundant) where unequal lifetimes of the ^{139}La Zeeman states, which are on the order of the reciprocal of the J coupling (~290 Hz), cause variable broadening of the multiplet lines (see Supporting Information Figure S35). The isotropic shift of the metal-bound silicon resonance in the ^{29}Si MAS NMR spectrum, $\delta_{iso\text{-}ss}$, is comparable but not identical to the corresponding signal seen in solution, $\delta_{iso\text{-}sol}$ ($\Delta_{sol\text{-}ss}$ = 19.5 ppm), which is indicative of a different Si environment. The ^{29}Si MAS NMR data of **1-La** can be compared with those recently reported for a series of La(III) Cp silanide anions, though for the majority of these complexes the metal-bound Si atom signals were resolved octets and J coupling constants could be extracted straightforwardly: $[La(Cp)_3(SiR_3)]^-$ (SiR_3 =

$Si(H)(C_6H_2Me_3\text{-}2,4,6)_2$, δ_{iso}: –36.0 ppm, $^1J_{LaSi}$ = 335 Hz; $Si(Me)Ph_2$, δ_{iso}: –1.7 ppm, $^1J_{LaSi}$ = 337 Hz; $SiPh_3$, δ_{iso}: 7.0 ppm, $^1J_{LaSi}$ = 318 Hz; $Si\{Si(H)Ph_2\}Ph_2$, δ_{iso}: –21.1 ppm, $^1J_{LaSi}$ not observed).[55] Only one signal was observed for the $SiMe_3$ groups of **1-La** at δ_{iso} = –4.6 ppm, which is at a similar chemical shift to the group 2 $SiMe_3$ groups in the solution ^{29}Si DEPT90 NMR spectrum (δ_{iso} = –5.3 ppm). However, given the good intensity and resolution of this spectrum and the clear absence of a second $SiMe_3$ signal, we posit that there is dynamic averaging of the $SiMe_3$ groups in the solid state at ambient temperature, as seen previously for a Cr(II) borylene complex, $[Cr\{=BSi(SiMe_3)_3\}(CO)_5]$.[56]

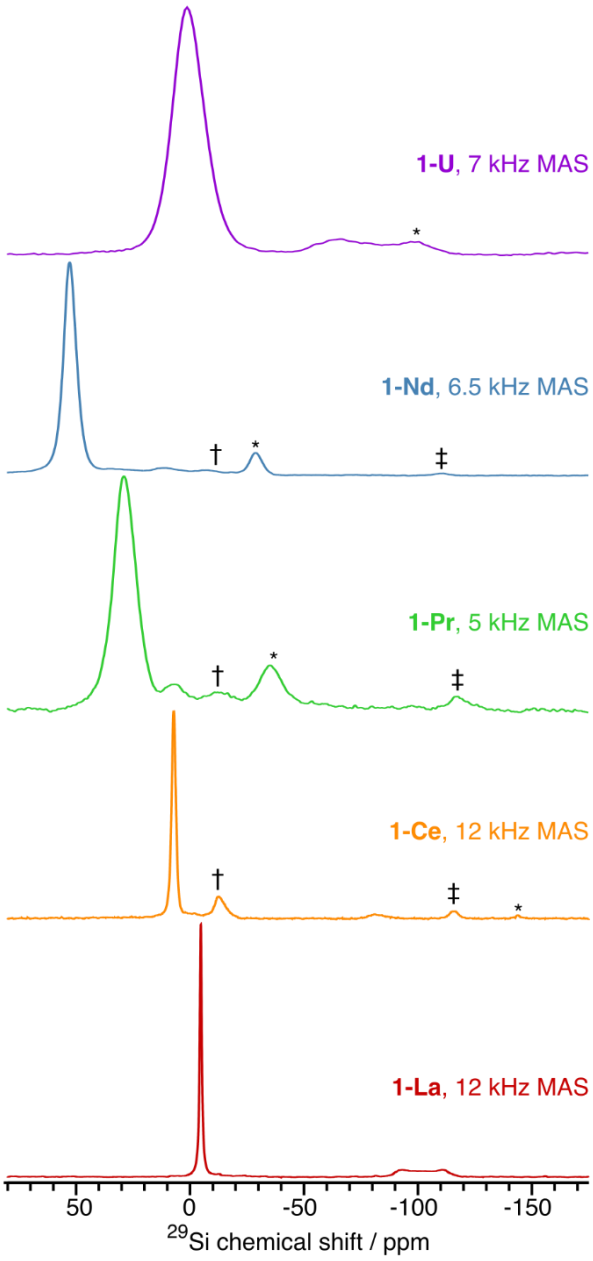

Figure 3. 9.4 T solid-state ^{29}Si MAS NMR spectra of **1-M** recorded at ambient temperature using the indicated MAS frequencies. The spectra of **1-La**, **1-Ce**, and **1-Pr** were recorded with $\{^{1}H–\}^{29}Si$ cross-polarization, whilst the spectra of **1-Nd** and **1-U** were recorded with direct ^{29}Si excitation. Asterisks (*) denote spinning side bands, whereas daggers (†) and double daggers (‡) denote $SiH(\mathit{Si}Me_3)_3$ and $\mathit{Si}H(SiMe_3)_3$ ^{29}Si resonances from a degradation product, respectively.

Table 3. Selected ssNMR parameters for **1-M**. δ_{iso} = isotropic shift; δ_{11}, δ_{22}, δ_{33} = principal components of chemical shift tensor; $^{1H}T_1$ = ^{1}H nuclei spin-lattice relaxation time constant, determined from a saturation-recovery experiment; $^{29Si}T_2$* = ^{29}Si apparent transverse relaxation time, determined from the peak FWHM. Note that the principal components of the chemical shift tensor are not definitive due to large relative errors in the fitting, particularly for δ_{22} and δ_{33}.

Complex	Resonance	^{29}Si δ_{iso} / ppm	^{29}Si δ_{11} / ppm	^{29}Si δ_{22} / ppm	^{29}Si δ_{33} / ppm	^{29}Si resonance FWHM / Hz	$^{29Si}T_2$* / ms	$^{1H}T_1$ / ms
1-La	M*Si*	–102.6						
	*Si*Me$_3$	–4.6	19	–16	–16	29	10.8	710 ± 1
1-Ce	*Si*Me$_3$	7.2	56	–18	–18	169	1.9	24 ± 1
1-Pr	*Si*Me$_3$	28.8	122	–18	–18	909	0.4	25 ± 2
1-Nd	*Si*Me$_3$	52.5	142	35	–20	516	0.6	20 ± 1
1-U	*Si*Me$_3$	1.1	79	–38	–38	1,377	0.2	3.9 ± 0.2

For all paramagnetic **1-M** we do not observe signals that can be reliably assigned to metal-bound Si atoms, with resonances in the expected region attributed to minor diamagnetic impurities in the sample including HSi(SiMe$_3$)$_3$[53] and another signal at –82 ppm that could not be identified. As the relaxation rate that causes paramagnetic broadening is $\propto 1/r^6$ (where r is the M–Si distance), we assume that the M*Si* signals are hidden in the baseline due to the degree of magnetic anisotropy of the M(III) ion; this is evidenced by the broad *Si*Me$_3$ resonances, e.g. **1-Ce** FWHM ≈ 4 kHz (32 ppm), **1-U** FWHM ≈ 25 kHz (200 ppm). In solution these effects are averaged due to molecular tumbling, allowing metal-bound Si resonances to be observed (see above). Only one signal associated with the SiMe$_3$ groups is seen in the ^{29}Si MAS NMR spectra of all paramagnetic **1-M**, consistent with the spectrum of **1-La** (see above); these signals are paramagnetically shifted from **1-La** to various extents depending on the identity of the M(III) ion (δ_{iso}{^{29}Si} = 7.2 ppm, **1-Ce**; 28.8 ppm, **1-Pr**; 52.5 ppm, **1-Nd**; 1.1 ppm, **1-U**), with the smaller magnetic anisotropy of Ce(III) resulting in a relatively sharp signal and the larger magnetic anisotropies of Pr(III), Nd(III) and U(III) giving broader resonances. These shifts essentially arise from a large deshielding of the δ_{11} component of the ^{29}Si chemical shift tensor (see Table 3), as the δ_{22} and δ_{33} components typically display negligible change (except for **1-Nd** and **1-U**). This infers a large anisotropy of the ^{29}Si chemical shielding of the SiMe$_3$ moieties and thus asymmetry of the electron distribution along the Si–Si bond, which is influenced by the f-block ion. For **1-Ln** the magnitude of the deshielding of the δ_{11} component is inversely proportional to the apparent ionic radius (taken from the M–Si bond distance, Table 1) of the f-ion (i.e. δ_{11}{^{29}*Si*Me$_3$} Nd > Pr > Ce > La). However, this is not the case for **1-U**, where a relative shielding of the δ_{22} and δ_{33}

components of the $^{29}SiMe_3$ groups is observed; this could arise from the intrinsic larger covalent effects of 5f *vs*. 4f orbitals, 6d mixing, or a spin-orbit coupling effect.

For the majority of paramagnetic **1-M**, the corresponding ^{1}H MAS NMR spectra are relatively uninformative (see Supporting Information Figure S40). However, resonances from metal-bound THF can be observed for **1-Ce** ($\delta_{iso}\{^1H\}$ = 11.3 and 5.9 ppm), which are clearly deshielded compared to those from **1-La** ($\delta_{iso}\{^1H\}$ = 5.2 and 2.6 ppm, see Supporting Information Figure S41), with the CH_2 protons either side of the O atom showing the largest shift. This arises from the proximity of these atoms to the paramagnetic Ce, and results in a large deshielding of the δ_{11} component of the CSA tensor (see Supporting Information Table S2); it appears that the corresponding δ_{22} component becomes more shielded.

UV-Vis-NIR Spectroscopy. Complexes **1-M** range in color from pale yellow (**1-La**) to dark green (**1-U**), thus UV-Vis-NIR spectra of **1-M** were recorded at room temperature as 2 mM THF solutions (Figure 4, see Supporting Information Figures S48-S52 for individual spectra); spectra were collected within 15 minutes of sample preparation at 0 °C thus complex solution equilibria are in operation and some sample decomposition will have occurred (see above), so we restrict our interpretation of these data accordingly. All spectra showed intense charge transfer (CT) absorptions tailing in from the UV region to various extents; for **1-La** a maximum was observed at $\tilde{\upsilon}_{max}$ = 27,150 cm^{-1} (ε = 1,760 M^{-1} cm^{-1}), and for **1-Ce** two shoulders were seen at $\tilde{\upsilon}_{max}$ = 26,750 cm^{-1} (ε = 1,010 M^{-1} cm^{-1}) and 23,300 cm^{-1} (ε = 240 M^{-1} cm^{-1}); the latter of these absorptions can be assigned to a $4f^1 \rightarrow 5d^1$ transition, as previously seen for [Ce(Cp″)$_2${Si(SiMe$_3$)$_3$}].[41] The spectra of **1-La**, **1-Ce** and **1-Pr** are otherwise featureless, whilst **1-Nd** additionally displays a weak set of absorptions in the visible region ($\tilde{\upsilon}_{max}$ = 17,250 cm^{-1}; ε = 30 M^{-1} cm^{-1}) that we assign as f-f transitions arising from the $^4I_{9/2} \rightarrow {}^4G_{5/2}$ states.[57] In contrast, **1-U** exhibits strong absorptions throughout the visible and NIR regions, which gradually decrease in intensity with increasing wavelength (e.g. $\tilde{\upsilon}_{max}$ = 20,500 cm^{-1}, ε = 1,420 M^{-1} cm^{-1}; $\tilde{\upsilon}_{max}$ = 8,650 cm^{-1}, ε = 120 M^{-1} cm^{-1}); similarly strong and broad absorptions were recently observed for [K(18-crown-6)][U{[Si(SiMe$_3$)$_2$SiMe$_2$]$_2$O}(THF)$_2$(I)$_2$] (e.g. $\tilde{\upsilon}_{max}$ = 17,240 cm^{-1}, ε = 1,250 M^{-1} cm^{-1}; $\tilde{\upsilon}_{max}$ = 13,330 cm^{-1}, ε = 820 M^{-1} cm^{-1}).[45] Whilst such features in U(III) complexes can be assigned as 5f→6d transitions,[1] they have previously been attributed to formally Laporte forbidden f-f transitions,[58-60] with the "intensity-stealing" due to significant mixing of U 5f orbitals with both 6d orbitals and ligand orbitals.[61-63]

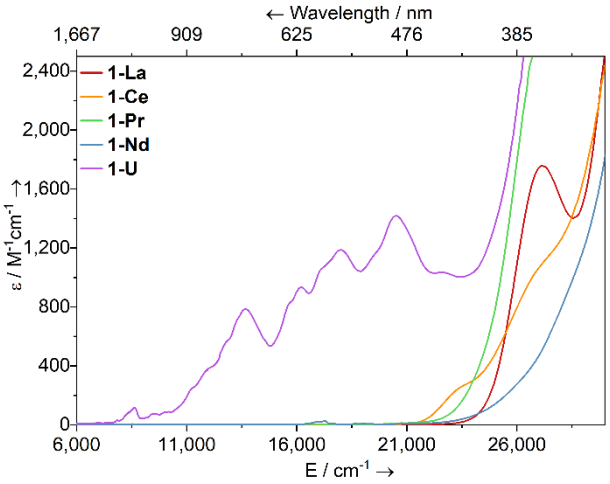

Figure 4. UV-Vis-NIR spectrum of **1-M** in THF (2 mM) between 6,000-30,000 cm^{-1} (1,667-333 nm). Legend: M = La (red), Ce (orange), Pr (green), Nd (blue), U (purple).

Magnetism. The effective magnetic moment (μ_{eff}) and molar magnetic susceptibility ($\chi_M T$) of powdered samples of paramagnetic **1-M** suspended in eicosane were examined by variable-temperature DC SQUID magnetometry and CASSCF-SO (see below) calculations (selected parameters compiled in Table 4, see Supporting Information Figures S68-S70 and Table S5 for all magnetic data). There is good agreement between measured and calculated magnetization values, and those expected for free M(III) ions Ce(III) ($4f^1$ $^2F_{5/2}$), Nd(III) ($4f^3$ $^4I_{9/2}$) and U(III) ($4f^3$ $^4I_{9/2}$). However, low magnetic susceptibility values were observed for several different batches of **1-Pr**; at 300 K the discrepancy between the experimental data presented and the expected value for a Pr(III) ion ($4f^2$ $^3H_4$) and the CASSCF-SO predicted value (see below) is *ca*. 0.3 cm^3 mol^{-1} K, which may warrant future investigation.[1] A gradual decrease in χT with temperature was observed for all **1-M**, due to thermal depopulation of excited crystal field states, with a sharper drop in χT < *ca.* 30 K attributed to poor thermal equilibration of the sample at lower temperatures. Magnetic saturation (M_{sat}) was not reached at 2 K for **1-Ce** or **1-Pr** in fields up to 7 T, but this was effectively reached for **1-Nd** and **1-U** under the same conditions, with 2 K and 4 K magnetization *vs*. field traces in good agreement with those calculated for **1-Ce**, **1-Nd** and **1-U**. Both **1-Nd** and **1-U** exhibit similar butterfly-shaped hysteresis loops at 2 K (see Supporting Information Figure S70).

Table 4. Powder magnetic moment and variable-temperature molar susceptibility, μ_{eff} (μ_B) and $\chi_M T$ ($cm^3\ mol^{-1}\ K$), of **1-M** measured by SQUID magnetometry at 1.8 and 300 K. $\chi_M T$ at 2 and 300 K determined by CASSCF-SO calculations, free ion calculated μ_{eff} and $\chi_M T$ values at 300 K.

Complex	SQUID Magnetometry				CASSCF-SO Calculations		Free ion at 300 K[1,2]	
	1.8 K		300 K		2 K	300 K		
	μ_{eff}	$\chi_M T$	μ_{eff}	$\chi_M T$	$\chi_M T$	$\chi_M T$	μ_{eff}	$\chi_M T$
1-Ce	0.45	0.03	2.33	0.68	0.23	0.70	2.54	0.81
1-Pr	1.68	0.35	3.07	1.18	0.56	1.55	3.58	1.60
1-Nd	0.82	0.08	3.60	1.62	1.15	1.64	3.62	1.64
1-U	1.11	0.16	3.38	1.43	1.16	1.46	3.62	1.64

EPR Spectroscopy. The electronic structures of the Kramers ion complexes **1-Ce**, **1-Nd** and **1-U** were probed further by continuous wave X-band (*ca.* 9.4 GHz) EPR spectroscopy, with spectra modelled using EasySpin.[64] The easy-axis powder EPR spectrum for **1-Ce** at 7 K (Table 5, see Supporting Information Figure S71) is best modelled as an effective $S = ½$ with $g_1 = 2.445$ and $g_2 = 0.786$ which are clearly observed, whilst $g_3 \sim 0.57$ is broadened into the baseline. An easy-axis powder EPR spectrum was also observed for **1-Nd** at 5 K, where hyperfine coupling to $I = 7/2$ ^{143}Nd (12.2%) and ^{145}Nd (8.3%) nuclei could be modelled for the sharp low-field feature ($g_1 = 6.26$, $A_1 = 1{,}860$ MHz) and a broad absorption at high field to account for g_2 (0.36), g_3 was not observed (< 0.4; Table 5, Figure 5). A frozen solution EPR spectrum of **1-Nd** in 2-Me-THF at 7 K reveals a sharp easy-axis component, consistent with the powder EPR spectrum, in addition to a broad rhombic signal spanning 115 – 850 mT with a peak centered at $g_1 \sim 4.8$, a broad derivative-like feature at $g_2 \sim 2.1$ and no resolved g_3 feature (broadened into g_2 or < 0.4; Table 5, Figure 5). The broad rhombic signal, which deviates significantly from the solid-state data, could arise from $Nd(THF)_n$ (n = 0 or 1) and/or a range of intermediate geometries; this assertion is supported by the significant change in the g-values of the ground Kramers doublet when THF ligands are removed, see below (see Supporting Information Table S23). The powder EPR spectrum of **1-U** is dominated by a broad feature from 100 – 600 mT that shows two lower-field features at $g \sim 6.6$ and 5.4 and contains a sharp organic radical signal at $g = 2.0023$ (Table 5, see Supporting Information Figure S72). This spectrum suggests the presence of multiple species from sample decomposition with allowed EPR transitions.

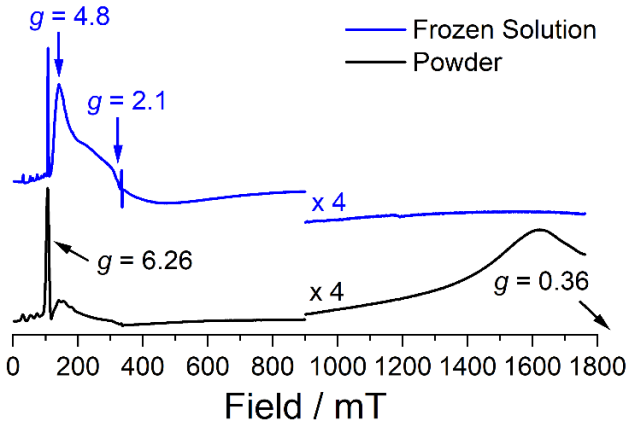

Figure 5. Comparison of X-band EPR spectra of **1-Nd** as a powder at 5 K (black) and as a frozen solution in 2-Me-THF at 7 K (blue).

Table 5. X-band EPR parameters of **1-Ce**, **1-Nd** and **1-U**.

Complex	State / Temperature	g_1	g_2	g_3	A_1 / MHz
1-Ce	Powder / 7 K	2.445	0.786	0.57	
	CASSCF/ -	2.378	0.946	0.715	
1-Nd	Powder / 5 K	6.26	0.36	-	1,860
	Solution / 7 K	~4.8	~2.1	-	
	CASSCF/ -	6.032	0.403	0.325	
1-U	Powder / 4 K	6.6, 5.4	-	-	
	CASSCF/ -	6.097	0.055	0.045	

DFT Calculations. We performed restricted spin orbit relativistic DFT calculations on diamagnetic **1-La** and $[La\{Si(SiMe_3)_3\}_3(THF)_n]$ (n = 0 or 1) using the Amsterdam Density Functional (ADF) suite version 2017 with standard convergence criteria,[65-67] in order to probe their electronic structures (see Experimental Section for details). The model for **1-La** used the metrical parameters observed by single crystal XRD with geometry-optimized H-atom positions, whilst in the absence of crystallographic metrical data the atomic positions of models of $La(THF)_1$ and $La(THF)_0$ desolvated analogues were fully geometry-optimized (see Supporting Information Tables S6-S8 for atomic coordinates of geometry-optimized structures). We calculated the δ_{Si} chemical shifts of both the metal-bound Si atoms and the $SiMe_3$ groups for **1-La**, $La(THF)_1$ and $La(THF)_0$ using BP86, PBE0, SAOP and B3LYP functionals, with a range of hybrid density functionals for the latter incorporating between 10 and 50% of the exact exchange energy from Hartree-Fock (HF) theory.[68] Whilst PBE0 has been used often to calculate NMR chemical shifts,[69-76] and SAOP often provides good correlation with experimental data despite being less computationally demanding,[46,77,78] we find that B3LYP with 40% HF exchange energy (B3LYPHF40) gives the best agreement for the complexes investigated herein, noting that in our

hands B3LYPHF20-40 calculations have well-reproduced experimental f-element-bound ^{13}C, ^{15}N, and ^{31}P chemical shift parameters.[79-81] Here we report mean values of calculated δ_{Si} chemical shifts for metal-bound Si atoms and weighted averages for those within $SiMe_3$ groups from all hypersilanide ligands to account for dynamic averaging (Table 6; see Supporting Information Tables S9-S14 for results from other functionals). However, we note that for **1-La**, $La(THF)_1$ and $La(THF)_0$ there are consistently two sets of predicted $SiMe_3$ ^{29}Si NMR signals in a 1 : 2 ratio separated by between 6-10 ppm, in agreement with the solution ^{29}Si DEPT90 NMR spectral data (Table 2).

Table 6. Experimental and weighted averages of calculated (using the B3LYPHF40 functional) isotropic ^{29}Si NMR chemical shifts (δ_{iso} in ppm *vs*. $SiMe_4$) for **1-La** and $[La\{Si(SiMe_3)_3\}_3(THF)_n]$ (n = 0, $La(THF)_0$; n = 1, $La(THF)_1$). δ_{11}, δ_{22}, δ_{33} = principal components of chemical shift tensor; Skew, $\kappa = [3(\delta_{22}–\delta_{iso})]/\delta_{11}–\delta_{33})$; Span, $\Omega = \delta_{11}–\delta_{33}$.

Complex	Resonance	^{29}Si (exp) δ_{iso} / ppm	^{29}Si (calcd) δ_{iso} / ppm	^{29}Si δ_{11} / ppm	^{29}Si δ_{22} / ppm	^{29}Si δ_{33} / ppm	Skew, κ	Span, Ω / ppm
1-La	M*Si*	–102.6[a]	–102.7	–44.5	–80.4	–183.2	0.48	138.75
	SiMe_3	–4.6[a]	4.0	16.4	5.9	–10.4	0.19	26.78
$La(THF)_1$	M*Si*	–82.3[b]	–69.2	–13.6	–44.2	–149.7	0.55	136.07
	SiMe_3	–13.1[b] (Group 1) –5.3[b] (Group 2)	2.1[c]	21.0[c]	1.4[c]	–16.2[c]	–0.06[c]	37.17[c]
$La(THF)_0$	M*Si*	–82.3[b]	–43.8	8.5	7.4	–147.3	0.99	155.84
	SiMe_3	–13.1[b] (Group 1) –5.3[b] (Group 2)	3.4[c]	20.1[c]	2.3[c]	–12.2[c]	–0.11[c]	32.22[c]

[a]Solid-state ^{29}Si MAS NMR data, corresponding to n = 2. [b]Solution ^{29}Si DEPT90 NMR data, corresponding to n = 1. [c]Only one value obtained upon averaging.

The computed MDC_q charges for La and Si_{Si3} (av.) in **1-La** are 1.14 and –0.47, consistent with their formal +3 and –1 charge states, and reflect net donation of electron density from the ligands to La. The mean Nalewajski-Mrozek La–Si bond indices are 0.56, reflecting the polar-covalent nature of those bonds; for comparison, the corresponding mean $La–O_{THF}$ and Si–Si values are 0.19 and 0.95.

The frontier Kohn-Sham molecular orbitals (KSMOs) of **1-La** (Figure S73) are as expected, with the HOMO to HOMO–2 reflecting the symmetric and anti-symmetric combinations of the three La–Si bonds. However, these KSMOs are rather delocalized, and so we turned to bond localization methods. The Natural Bond Orbital (NBO) method[82] finds three essentially identical La–Si bonds (Figure S74) of 11 and 89% La and Si character, respectively. The La components are comprised of 25/1/71/3% s/p/d/f character and the Si contributions are 40/60% s/p character;

similar orbital breakdowns have previously been calculated for other La silanide complexes.[55] These data are very similar to the Natural Localized Molecular Orbital (NLMO) representations of **1-La** (Figure S75), which return 11 and 87% La and Si character, respectively. The La and Si components are 35/1/62/2% s/p/d/f and 41/59% s/p. Thus, whilst the NLMO report increased s-character at the expense of d-contributions for La compared to the NBO interpretation, a fairly consistent bonding picture emerges of La binding to sp hybridized Si atoms utilizing sd^3 hybrid orbitals.

We examined the La–Si bond topologies of **1-La** using the Quantum Theory of Atoms in Molecules (QTAIM)[83,84] and found three essentially identical La–Si 3,–1-bond critical points. These exhibit ρ, $\nabla^2\rho$, H, and ε values of 0.04, 0.02, –0.01, and 0.11. These reflect rather polar and weak La–Si interactions, since covalent bonds tend to have ρ values >0.1 and more negative H terms. The ε term is normally zero, or close to zero, for single and triple bonds, with larger values for double bonds;[85] the modest ε values here reflect that the silanide ligands each bind to the La center in a slightly skewed manner, which is apparent in the NBO and NLMO visualizations of **1-La** (Figures S74 and S75), and thus their bond ellipticities are not ideal.

Ab initio Calculations. The electronic structures of paramagnetic **1-M** were investigated by minimal active space CASSCF-SO calculations using OpenMolcas (see Experimental Section and Supporting Information Tables S15-S18 for details).[86] The ground state for **1-Ce** is dominated by $|\pm 3/2\rangle$ (97%) making it only weakly magnetic with $g_1 = 2.38$, $g_2 = 0.95$, $g_3 = 0.71$, where the largest *g*-value is coincident with the O–Ce–O axis, suggesting that the intermediate $|\pm 3/2\rangle$ m_J state is stabilized[87,88] by competition between the hard Lewis base O-donor atoms of THF and the equatorial field imposed by the three softer silanide ligands. The calculated *g*-values are in good agreement with experimental EPR data (Table 5). The CASSCF-SO ground state of **1-Pr** is a mixed $49\%|\pm 4\rangle + 49\%|\mp 4\rangle$ pseudo-doublet with a splitting of 6 cm^{-1}. The principal magnetic axis is coincident with O–Pr–O, indicating the oblate spheroid $|\pm 4\rangle$ m_J state is stabilized[87,88] by O-donor atoms of THF to a greater extent than the silanide ligands. The ground state for **1-Nd** is relatively high purity ($90\%|\pm 9/2\rangle + 7\%|\pm 5/2\rangle + 3\%|\mp 3/2\rangle$) with $g_1 = 6.03$ and $g_{2,3} < 0.4$. Similarly for **1-U**, a relatively pure ground doublet was found ($89\% |\pm 9/2\rangle + 11\% |\pm 5/2\rangle$). The EPR data for **1-U** exhibits overlapping features from decomposition products that obscure the spectrum, although features observed at $g = 6.6$ and 5.4 are comparable to the calculated axial *g*-value (Table 5). The orientation of the magnetic axes for the $m_J = 9/2$ Kramers doublets for **1-Nd** and **1-U** are the same as for **1-Pr** and **1-Ce**.

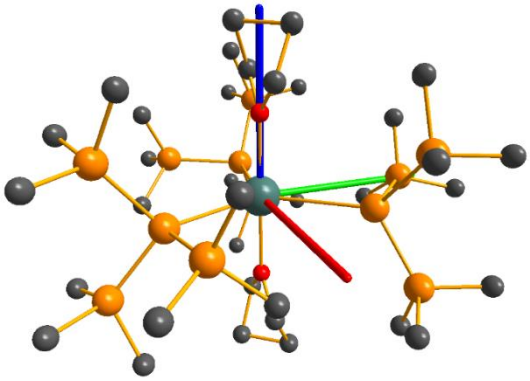

Figure 6. CASSCF-SO-calculated magnetic axes for **1-Ce** (blue: g_1, most magnetic; green: g_2, intermediate; red: g_3, least magnetic) for complexes. Metal, silicon, carbon, and hydrogen atoms shown as metallic green, orange, grey, and light grey respectively.

pNMR calculations. We calculated the pNMR shifts using two methods (see Experimental Section for details): (i) a point-dipole approximation based on the CASSCF-SO-calculated magnetic susceptibility tensor (pseudo-contact shift (PCS) approximation, $\delta_{\mathrm{PCS}}^{\mathrm{para}}$);[89] and, (ii) a full sum-over-states expression derived from the derivative of the Helmholtz free energy (van den Heuvel and Soncini's method $\delta_{\mathrm{vdH-S}}^{\mathrm{para}}$).[47] The latter method is calculated directly based on the CASSCF-SO wavefunction and implicitly includes all through-bond (i.e. contact) and through-space (i.e. pseudo-contact) terms, as well as the relativistic paramagnetic spin-orbit (PSO) terms.[90] To calculate the experimental paramagnetic shift $\delta_{\mathrm{exp}}^{\mathrm{para}}$, we subtracted the diamagnetic NMR signals measured for **1-La** from the respective signals in the paramagnetic compounds. We report calculated δ^{para} values obtained by averaging the calculated shift for all atoms in the same chemical environment, to approximate conformational averaging in the solution phase. We performed calculations using the XRD structure as well as a gas-phase optimized geometry (which retains the same disposition of ligands as in the XRD structure), and model compounds with one or two THF molecules removed (see Experimental Section for details). Upon dissociation of one THF, the central $M(Si)_3$ core slightly pyramidalizes and the M–Si bond lengths decrease, which becomes more pronounced when the second THF is displaced (see Supporting Information Tables S19-S21). As suspected, removing THF ligands from **1-M** changes the magnetic anisotropy; this is most clearly observed in the effective *g*-values of the ground Kramers doublets in **1-Ce** and **1-Nd**, which change from easy-axis anisotropy when there are two THF ligands coordinated, to rhombic anisotropy with one THF, and finally to easy-plane anisotropy when both THF ligands are removed (see Supporting Information Tables S22 and S23).

For calculation of δ^{para} in the M(THF)$_1$ and M(THF)$_0$ structures, there are several models that can be used to account for the solution ^{1}H NMR spectra of **1-M** showing a 2:1 ratio for the SiMe$_3$ signals. For the M(THF)$_1$ structures, one can consider one SiMe$_3$ group of each hypersilanide ligand on the same side of the M(Si$_M$)$_3$ plane as the remaining THF ligand ("cis") and the other two SiMe$_3$ groups on the opposite side ("trans"), as well as the opposite arrangement (two "cis" and one "trans"). For the M(THF)$_0$ structures, one can consider one SiMe$_3$ group of each hypersilanide ligand closer to the pyramidalized M atom ("proximal"), and the other two further away ("distal"), or vice-versa (two "proximal" and one "distal"). In some of our model structures the assignment is not obvious between the three ligands, thus to address this uncertainty, and to account for dynamic rotation of each of the σ-bonds in the hypersilanide framework, we have used three approaches to account for all the possible scenarios. We define the "plane" as the average plane formed by the four M(Si$_M$)$_3$ atoms, and then determine which non-bound Si atom on each ligand is closest to the plane. In the first approach, these are defined as the group 1 ("in-plane") SiMe$_3$ groups, and the other two as the group 2 ("out-of-plane") groups (see Supporting Information Tables S24-S26). In the second approach, we located the non-bound Si atoms that are farthest from the plane to define group 1, whereas the other two Si atoms that are closer to the plane are defined as group 2 (see Supporting Information Tables S27-S29). In the third approach, we consider the only remaining option for a 2:1 ratio, which is where the SiMe$_3$ group closest to the plane is averaged with the one that is farthest from the plane to define group 2, and the intermediate SiMe$_3$ group defines group 1 (see Supporting Information Tables S30-S32).

Discussion

Calculation of the ssNMR data for **1-La** using DFT methods (see Experimental Section) gives mean isotropic ^{29}Si NMR chemical shifts of δ_{iso} = –102.7 ppm for the metal-bound Si atoms, in excellent agreement with the experimentally observed ^{29}Si MAS NMR shift of –102.6 ppm. The weighted average of the calculated SiMe$_3$ ^{29}Si shifts for **1-La** (δ_{iso} = 4.0 ppm) has a slightly worse agreement with the experimental ssNMR value of –4.6 ppm, suggesting that ambient temperature dynamics may need to be considered. Though there is little variance in the mean calculated ^{29}Si δ_{iso} values of SiMe$_3$ groups between **1-La** and desolvated La(THF)$_0$ and La(THF)$_1$ (Table 6), the mean of the calculated ^{29}Si NMR shifts for the metal-bound Si atoms of **1-La** and desolvated La(THF)$_1$ of δ_{iso} = –85.9 ppm is similar to the experimentally-obtained solution ^{29}Si DEPT NMR value (δ_{iso} = –82.3 ppm); we note that the calculated δ_{iso} = –43.8 ppm for the metal-bound Si atoms of the La(THF)$_0$ derivative, which has worse agreement with experiment. Furthermore, the difference in δ_{Si} values of Group 1 and Group 2 SiMe$_3$ groups obtained from a 9 : 1 C$_6$D$_6$: C$_4$D$_8$O

solution of **1-La** at room temperature ($\Delta SiMe_3$ = 7.8 ppm) is close to the mean ($\Delta SiMe_3$ = 8.1 ppm) of equivalent differences calculated for **1-La** ($\Delta SiMe_3$ = 9.9 ppm; δ_{iso} = –2.6 and 7.3 ppm) and its $M(THF)_1$ analogue ($\Delta SiMe_3$ = 6.3 ppm; δ_{iso} = –2.1 and 4.2 ppm). These data are in accord with **1-La** forming a dynamic equilibrium with the desolvated $La(THF)_1$ form and deuterated analogues in the solution NMR experiments. We therefore posit that the presence of two signals for $SiMe_3$ groups in solutions of **1-M** is due to restricted rotation of the M–Si bonds, likely due to the desolvated species showing stronger interactions of coordinatively unsaturated M(III) ions with hypersilanide ligands and the resultant metal coordination spheres being more congested, consistent with the optimized gas-phase geometries.

The solid-state magnetic and EPR data of paramagnetic **1-M** are consistent with the CASSCF-SO calculations performed on the solid-state XRD structures, which show easy-axis magnetic ground states in all cases, seemingly dictated by the axial THF ligands (Figure 6). As with the solution NMR data of diamagnetic **1-La** (see above), the solution EPR and NMR data of paramagnetic **1-M** indicate that THF may be lost in solution, and this scenario can be probed further by analysis of the solution phase pNMR shifts. Although solvent effects were included for the DFT calculations of **1-La** by introducing a benzene continuum, they were not for the *ab initio* calculations of paramagnetic **1-M**. For the pNMR calculations we just used the gross local structure, as this has the largest effect on the magnetic anisotropy and hence pNMR shifts; the dynamic THF equilibrium will have a far greater influence than "outer sphere" solvent effects. We focus here on pNMR shifts of **1-Ce**, **1-Pr** and **1-Nd**, which have simpler electronic structures than **1-U** (Figure 4).[91]

Comparing the two CASSCF-SO-based theoretical methods for calculation of pNMR shifts to the solution data of paramagnetic **1-Ln** (see Supporting Information Tables S24-S32) we find that the δ_{PCS}^{para} and δ_{vdH-S}^{para} values are in close agreement for all ^1H pNMR signals, which is to be expected as these nuclei are far away from the spin density of the buried 4f orbitals. However, the PCS approximation will be less accurate for nuclei closer to the metal ion where delocalization of spin-density is non-zero, and indeed this is what we observe for the ^{29}Si pNMR shifts, even for the non-coordinated ^{29}Si nuclei. The ^{29}Si NMR resonances of the metal-bound silicon atoms are hugely sensitive to contact shift, which we are not able to calculate well. The contact shift contribution to chemical shift is non-trivial, arising from core spin polarization and dynamic electron correlation, intersecting with relativistic core effects, thus we cannot rationalize any trends.

Comparing the experimental solution phase ^1H δ_{exp}^{para} to the calculated δ^{para} results using either XRD or gas-phase optimized structures, we find that the group 1 $SiMe_3$ shifts have the incorrect sign and the group 2 $SiMe_3$ shifts are under-predicted in magnitude by several ppm (see Supporting Information Tables S24-S26). As the solution pNMR

data show local C_{3v} point symmetry of the complex (borne out as a 1 : 2 ratio of the $SiMe_3$ ^1H signals, *viz*. groups 1 and 2, respectively, with restricted rotation around the M–Si bonds due to steric clashing in the presence of shorter M–Si bonds), the molecules must possess axially symmetric magnetic anisotropy. Furthermore, owing to the good applicability of the PCS approximation for the ^1H nuclei in this case (i.e. the difference between $\delta_{\mathrm{PCS}}^{\mathrm{para}}$ and $\delta_{\mathrm{vdH-S}}^{\mathrm{para}}$ is small), we can therefore write $\delta_{\mathrm{PCS}}^{\mathrm{para}} = \frac{\chi_z - \bar{\chi}}{2N_A}\frac{3cos^2\theta - 1}{r^3}$.[89] Because the $\delta_{\mathrm{exp}}^{\mathrm{para}}$ are positive for the group 1 and negative for the group 2 ^1H nuclei, and $\chi_z - \bar{\chi}$ is a constant common to both sets of ^1H environments, then the structural part $\frac{3cos^2\theta - 1}{r^3}$ must have a different sign for each group of protons. Assuming first that the disposition of the $SiMe_3$ groups does not change significantly in solution, the group 1 "in-plane" protons would on average be closer to θ = 90°, whilst the group 2 "out-of-plane" protons would be closer to θ = 0° or θ = 180°. This indicates that the structural part of the term for group 1 is < 0 while for group 2 it is > 0, and thus $\chi_z - \bar{\chi}$ must be < 0 to be consistent with $\delta_{\mathrm{exp}}^{\mathrm{para}}$. This implies easy-plane anisotropy of the magnetic moment, which would indeed be consistent with Ln(III) ions for Ln = Ce, Pr and Nd with a trigonal planar ligand field dominated by the three anionic equatorial ligands.[87] However, CASSCF-SO calculations using the XRD structure predict easy-axis anisotropy for **1-Ce**, **1-Pr** and **1-Nd**, dictated by the axial THF ligands (see above; the outcome does not change for the gas-phase optimized structures), which is indeed confirmed by EPR spectroscopy on solid state samples. This apparent disconnect could be resolved if one or both THF molecules dissociate in solution, which is already suggested by missing solution ^1H resonances for some of the THF ligands and **1-La** results (see above). Hence, we computationally removed one or both THF ligands(s), optimized the structure in the gas phase, and performed CASSCF-SO pNMR calculations for these structural models to assess if this possibility is consistent with the data.

For **1-Ce** none of the pNMR shift calculations give a clear agreement with solution experimental data (see Supporting Information Tables S24, S27 and S30); as Ce(III) has the smallest magnetic moment of all Ln(III) ions in the periodic table it also has the smallest paramagnetic shifts, and hence approximations in our electronic structure method and our gas-phase structural models are insufficient to capture the subtleties of these data. Considering **1-Nd**, both ^1H and ^{29}Si solution pNMR results show discrepancies between the experimental values and the values predicted using the XRD or optimized $M(THF)_2$ structures. For the ^1H resonances, calculations using the XRD structure (optimized structure) predict shifts of –6.4 and *ca*. –0.5 ppm (–2.3 and *ca*. –0.4 ppm) for the "in-plane"/group 1 and "out-of-plane"/group 2 signals, respectively, compared to the experimental values of 4.9 and –5.0 ppm, respectively. Upon removing one THF ligand and maintaining the "in-plane"/"out-of-plane" averaging, the calculations give chemical

shifts of *ca*. 5.8 and –4.2 ppm, respectively, or *ca*. 5.8 and –5.6 ppm when both THF ligands are removed (see Supporting Information Table S26). For the ^{29}Si "in- plane"/group 1 resonances (group 2 not observed; now considering only $\delta^{\mathrm{para}}_{\mathrm{vdH-S}}$), the predicted shift using the XRD structure (optimized structure) is –22.3 ppm (–11.7 ppm), which varies from the experimental value of 6.3 ppm. When one THF ligand is removed the shift increases to 8.7 ppm, and then to 8.0 ppm when the second THF ligand is removed (see Supporting Information Table S26). Hence, both the ^{1}H and ^{29}Si pNMR data suggest a formulation of either Nd(THF)$_1$ or Nd(THF)$_0$ for **1-Nd** in solution. All chemical shifts show pronounced discrepancy compared to experiment for the second averaging option (see Supporting Information Table S29), whilst the third averaging option (see Supporting Information Table S32) is also compatible with Nd(THF)$_1$; however, the agreement of calculated values with experiment is not as close as for "in-plane"/"out-of-plane" averaging.

For **1-Pr**, both ^{1}H and ^{29}Si calculated pNMR results show discrepancies compared to the experimental solution values when employing *bis*-THF structures (see Supporting Information Table S25). Using the XRD structure (optimized structure) for ^{1}H gives shifts of *ca*. –14.5 and *ca*. –1.9 ppm (*ca*. –4.4 and *ca*. –0.5 ppm) for the "in-plane"/group 1 and "out-of-plane"/group 2 signals, respectively, compared to the experimental values of 7.9 and –8.1 ppm, respectively. By removing one THF ligand and maintaining the "in-plane"/"out-of-plane" averaging, the calculations give chemical shifts of *ca*. 11.0 and *ca*. –8.0 ppm, or *ca*. 7.6 and *ca*. –6.2 ppm when removing the second THF ligand (see Supporting Information Table S25). Hence, the models with some THF lost better align with the experimental data. Similarly, for solution ^{29}Si pNMR "in- plane"/group 1 resonances (group 2 not observed; now considering only $\delta^{\mathrm{para}}_{\mathrm{vdH-S}}$), the XRD structure (optimized structure) gives a shift of –40.9 ppm (optimized structure: –15.0 ppm), deviating substantially from the experimental value of 10.2 ppm. The shifts for Pr(THF)$_1$ and Pr(THF)$_0$ are 24.0 ppm and 16.0 ppm, respectively; here, the Pr(THF)$_0$ model is in better agreement with the experimental data (see Supporting Information Table S25). Using the second averaging method, the pNMR shifts are predicted adequately using a Pr(THF)$_0$ model (see Supporting Information Table S28), or using a Pr(THF)$_1$ model with the third averaging method (see Supporting Information Table S31), but in both cases the calculated parameters are not as close to experiment as for the "in-plane"/"out-of-plane" averaging approach.

We note that in none of the cases are the pNMR shifts of the coordinated ^{29}Si$_M$ atoms correctly predicted for paramagnetic **1-Ln**, and that the choice of structural model has a significant effect on the calculated values (see Supporting Information Tables S24-S26). This indicates substantial influence of the contact spin density based on structural models that we cannot capture with these simplified static models and minimal CASSCF-SO calculations. For paramagnetic **1-Ln**, only one non-metal-bound ^{29}Si resonance is observed, again likely a result of dynamic averaging.

The weighted average paramagnetic shifts are 11.8, 33.4 and 57.1 ppm for **1-Ce**, **1-Pr** and **1-Nd**, respectively, while the calculated pNMR shifts using the XRD geometries and CASSCF-SO methods (δ^{para}_{vdH-S}, weighted average of non-metal-bound ^{29}Si resonances) are –4.8, –23.6 and –13.8 ppm, for **1-Ce**, **1-Pr** and **1-Nd**, respectively. Clearly, these values are very poorly predicted, which shows that non-trivial spin density is transferred from the metal ions beyond the first coordination sphere and that extensive active space methods would be required to approach experimental accuracy in even these simple complexes.

The ^{29}Si NMR chemical shifts of a number of uranium complexes have previously been compiled, and though there is no ^{29}Si NMR data of a U(III) hypersilanide complex for comparison we note that $SiMe_3$ groups were assigned in the ^{29}Si NMR spectra of [K(18-crown-6)][U{[Si(SiMe$_3$)$_2$SiMe$_2$]$_2$O}(THF)$_2$(I)$_2$] (–50.0 ppm),[45] and trigonal pyramidal [U{N(SiMe$_3$)$_2$}$_3$] (–219 ppm).[92] The δ_{Si} values of the $SiMe_3$ groups (–6.0 ppm) and metal-bound silicon atoms (–70.5 ppm) of U(THF)$_n$ (n = 0 or 1) are far downfield of most of the previously reported range of δ_{Si} values for U(III) complexes (between –116 and –247 ppm), which tend to exhibit chemical shifts >100 ppm upfield of parent group 1 ligand transfer agents.[92] The comparatively small paramagnetic shift of the $SiMe_3$ groups and the silanides in U(THF)$_n$ (n = 0 or 1) from HSi(SiMe$_3$)$_3$ (δ_{Si} in C_6D_6 = –11.6 ppm, $SiMe_3$; –115.6 ppm, HSi)[53] correlates with the paramagnetic line broadening being relatively minor in the M(THF)$_n$ (n = 0 or 1) series herein, which delivers the first examples of M(III)-bound solution ^{29}Si DEPT90 NMR resonances for all of the paramagnetic M herein to the best of our knowledge (we note that a signal was tentatively assigned for the silanide atom in [La(Cp″)$_2${Si(SiMe$_3$)$_3$}] at δ_{Si} = –130.25 ppm, but data from correlation experiments were ambiguous).[41]

Conclusions

The rich multinuclear solution and ssNMR spectra of the M(III) *tris*-hypersilanide complexes [M{Si(SiMe$_3$)$_3$}$_3$(THF)$_2$] for M = La, Pr, Ce, Nd and U, coupled with the high local symmetries of their metal sites, has provided a rare opportunity to study paramagnetic shifts in an isostructural series of f-block complexes by ^{29}Si NMR spectroscopy. We find by a combination of single crystal XRD and EPR spectroscopy that in the solid state these complexes show trigonal bipyramidal geometries, with local D_{3h} symmetries of the central MSi_3O_2 cores and easy-axis magnetic anisotropy. The ^{29}Si MAS NMR spectra of these complexes each show only one signal for the trimethylsilyl groups; this equivalency indicates that dynamic averaging of these environments occurs at ambient temperature due to free rotation of M–Si bonds. The ^{29}Si resonance for the metal-bound silicon atoms is only seen for the diamagnetic La(III) analogue in the solid state, due to the magnetic anisotropy of the paramagnetic M(III) ions broadening the signal into the baseline. Using

a combination of characterization methods, we find that the coordinated THF molecules in [M{Si(SiMe$_3$)$_3$}$_3$(THF)$_2$] are readily displaced in solution to give the desolvated species [M{Si(SiMe$_3$)$_3$}$_3$(THF)$_n$] (n = 0 or 1), which show local C_{3v}-symmetric cores and easy-plane magnetic anisotropy. The solution ^{1}H NMR spectra of [M{Si(SiMe$_3$)$_3$}$_3$(THF)$_2$] in 9 : 1 C_6D_6 : C_4D_8O solutions each show two trimethylsilyl environments in a 1 : 2 ratio, and for M = La and Ce we also observe two signals for SiMe$_3$ groups in both the ^{13}C{^{1}H} and ^{29}Si DEPT solution NMR spectra. We attribute this observation to restricted rotation of M–Si bonds on the NMR timescale upon loss of THF from coordination spheres; unusually, metal-bound silicon resonances are seen in all solution ^{29}Si DEPT90 NMR spectra.

The DFT-calculated ^{29}Si NMR shifts of [La{Si(SiMe$_3$)$_3$}$_3$(THF)$_2$] and desolvated [La{Si(SiMe$_3$)$_3$}$_3$(THF)$_n$] (n = 0 or 1) showed excellent agreement with experimentally-obtained values, and were in accord with a dynamic equilibrium of [La{Si(SiMe$_3$)$_3$}$_3$(THF)$_2$] and [La{Si(SiMe$_3$)$_3$}$_3$(THF)] persisting in the presence of a large excess of THF. The CASSCF-SO-calculated pNMR shifts of trimethylsilyl groups in paramagnetic [M{Si(SiMe$_3$)$_3$}$_3$(THF)$_2$] and desolvated [M{Si(SiMe$_3$)$_3$}$_3$(THF)$_n$] (n = 0 or 1) show reasonable agreement for M = Pr and Nd existing as either [M{Si(SiMe$_3$)$_3$}$_3$(THF)$_1$] or [M{Si(SiMe$_3$)$_3$}$_3$] in 9 : 1 C_6D_6 : C_4D_8O solutions, but assigning the experimental data to one of these two structures is challenging given the likelihood of dynamic equilibria in solution, *cf*. the La homologue. We also cannot rule out the limitations inherent to the computational method used; for instance gas-phase optimization do not consider the effect of explicit solvent interaction which is in a huge excess for experimentally-obtained data. Furthermore, the experimental chemical shifts represent an average over large number of molecules that move over a relativity long time scale, as opposed to the chemical shift from single stationary molecule optimized in the gas phase as computed here; the time scales required for examining these equilibria are out of reach for the *ab initio* molecular dynamics that would be required to model the M-THF dissociation processes. Finally, the structural ambiguity and complex nature of the paramagnetic shifts does not allow us to accurately model metal-bound silicon atoms directly for any of the paramagnetic complexes herein.

Experimental Section

General methods and materials. All manipulations were conducted under argon with the strict exclusion of oxygen and water by using Schlenk line and glove box techniques. Solvents were dried by refluxing over Na/K alloy (diethyl ether) or potassium (hexane), and stored over a potassium mirror, then degassed before use. To make up solution samples for NMR, EPR and UV-Vis-NIR spectroscopy, hexane, toluene, THF, Me-THF, C_6D_6 and C_4D_8O were dried by refluxing over K, and were vacuum transferred and degassed by three freeze-pump-thaw cycles before use. Elemental

analysis (C, H) was carried out either by Mr Martin Jennings and Mrs Anne Davies at the Microanalytical service, Department of Chemistry, the University of Manchester, or the Elemental Analysis Services Team, Science Centre, London Metropolitan University. The starting materials [K{Si(SiMe$_3$)$_3$}],[54] [MI$_3$(THF)$_x$] (M = La, Ce, Pr, x = 4; M = Nd, x = 3.5)[93] and [UI$_3$(THF)$_4$][94] were prepared according to literature procedures. ATR-IR spectra were recorded as microcrystalline powders using a Bruker Alpha spectrometer with Platinum-ATR module. UV-Vis-NIR spectroscopy was performed on samples in Youngs tap-appended 10 mm path length quartz cuvettes on an Agilent Technologies Cary Series UV-Vis-NIR spectrophotometer from 175-3300 nm. *Caution: Natural abundance uranium is a weak α-emitter, thus we recommend the use of suitable designated radiochemical laboratories with α-counting equipment available for safe manipulation of compounds containing this element*.

Powder XRD data were obtained on small batches of microcrystalline **1-M** that were suspended in Fomblin® oil to prevent sample decomposition from oxygen and water. These samples were mounted on a Micromount™ and placed on a goniometer head under a cryostream to cool the sample to 100 K, freezing the Fomblin® to suspend the crystallites for the duration of the experiment. The PXRD data were measured on a Rigaku FR-X diffractometer, operating in powder diffraction mode using Cu Kα radiation (λ = 1.5418 Å) with a Hypix-6000HE detector and an Oxford Cryosystems nitrogen flow gas system. Data were collected between 3-20 °θ, with a detector distance of 150 mm and a beam divergence of 1.5 mRad.[95] X-ray data were collected using CrysAlisPro.[96] For data processing the instrument was calibrated using silver behenate as standard. Then, X-ray data were reduced and integrated using CrysAlisPro.[96] Pawley refinements with the unit cells obtained from the crystal structures were performed using TOPAS.[97,98]

X-ray diffraction data for single crystals of **1-La**, **1-Ce**, **1-Pr**, **1-Nd** and **1-U** in Fomblin® on a Micromount™ were examined using a Rigaku FR-X diffractometer, equipped with a HyPix 6000HE photon counting pixel array detector with graphite-monochromated Mo Kα (λ = 0.71073 Å) (**1-U**) or Cu Kα (λ = 1.5418 Å) (**1-La**, **1-Ce**, **1-Pr**, **1-Nd**) radiation. Intensities were integrated from data recorded on 1° frames by ω rotation. Cell parameters were refined from the observed positions of all strong reflections in each data set. A Gaussian grid face-indexed with a beam profile was applied for all structures.[96] The structures were solved using SHELXT;[99] the datasets were refined by full-matrix least-squares on all unique F^2 values,[100] with anisotropic displacement parameters for all non-hydrogen atoms, and with constrained riding hydrogen geometries; U_{iso}(H) was set at 1.2 (1.5 for methyl groups) times U_{eq} of the parent atom. The largest features in final difference syntheses were close to heavy atoms and were of no chemical significance.

CrysAlisPro[96] was used for control and integration, and SHELX[99,100] was employed through OLEX2[101] for structure solution and refinement. ORTEP-3[102] and POV-Ray[103] were employed for molecular graphics.

Solution NMR spectra were recorded on a Bruker AVIII HD 400 spectrometer operating at 400.07 (^{1}H), 100.60 (^{13}C), or 79.48 (^{29}Si) MHz; sample concentrations used were ~50 mM. All solution NMR spectra (^{1}H, ^{13}C, ^{29}Si) were referenced to tetramethylsilane (TMS). Solid-state ^{1}H, ^{29}Si direct excitation, and {^{1}H-}^{29}Si cross-polarization (CP) NMR spectra were recorded using a Bruker 9.4 T (400 MHz ^{1}H Larmor frequency) AVANCE III spectrometer equipped with a 4mm HFX MAS probe. Experiments were acquired at ambient temperature using various MAS frequencies. For the frequencies employed (5 to 12 kHz), the sample temperature was determined using an external reference of KBr to be 300 ± 3 K. Samples were packed into 4mm o.d. zirconia rotors in a glovebox, and sealed with a Kel-F rotor cap. The ^{1}H ($\pi/2$)- and π-pulse durations were 2.5 and 5.0 μs, respectively, and the ^{29}Si ($\pi/2$)- and π-pulse durations were 5.5 and 11.0 μs, respectively. ^{29}Si spin-locking was applied for 4 ms at ~45 kHz, with corresponding ramped (70–100%) ^{1}H spin-locking at 50–60 kHz (depending on MAS frequency) for CPMAS experiments. 100 kHz SPINAL-64[104] heteronuclear ^{1}H decoupling was used throughout signal acquisition. A Hahn-echo τ_r–π–τ_r sequence of two rotor periods total duration was applied to ^{29}Si after CP to circumvent receiver dead-time for **1-La**. 1312, 20768, 189440, 61440, and 22796 transients were co-added for **1-La**, **1-Ce**, **1-Pr**, **1-Nd**, and **1-U**, respectively, with repetition delays of 3, 0.2, 0.03, 0.2 and 0.2 s, respectively. Spectral simulations were performed in the solid line-shape analysis (SOLA) module v2.2.4 in Bruker TopSpin v4.0.9. All ssNMR spectra were referenced to TMS (^{1}H and ^{29}Si). Experiments were acquired at ambient temperature using various MAS frequencies. For the frequencies employed (5 to 12 kHz), the sample temperature was determined using an external reference of KBr to be 301 ± 10 K.

Magnetic measurements were performed on a Quantum Design MPMS3 superconducting quantum interference device (SQUID) magnetometer. Finely ground powder samples (28-36 mg) were restrained in eicosane (14-18 mg) and flame sealed in a borosilicate tube under vacuum (see Supporting Information Table S5). Sealed samples were loaded into plastic straws and held in place by friction between diamagnetic tape at the top of the tube and the straw. Raw magnetic data were scaled for the shape of the sample using Quantum Design MPMS3 Geometry Correction Simulator, corrected for the diamagnetic contribution of the sample holder (straw and borosilicate tube) and corrected for the mass of eicosane. The molar susceptibility was corrected for the intrinsic diamagnetic contribution of the sample, estimated as the molecular weight (g mol^{-1}) multiplied by 0.5×10^{-6} cm^3 K mol^{-1}.[105] Measurements were performed in DC scan mode with 40 mm scan length, except susceptibility measurements on **1-Ce** and **1-Pr** which were performed in VSM mode with 5 mm amplitude. Susceptibility measurements were performed on cooling in 5 kOe (**1-Ce**) or 1 kOe (**1-Pr**,

1-Nd, **1-U**) DC field. Hysteresis measurements were performed at 2 K in continuous sweep mode with sweep rates of 91 Oe s^{-1} ($2 < |H| < 7$ T), 54 Oe s^{-1} ($1 < |H| < 2$ T) and 22 Oe s^{-1} ($|H| < 1$ T).

Continuous wave electron paramagnetic resonance (EPR) spectra were recorded at X-band (*ca.* 9.4 GHz) frequency on a Bruker EMXPlus spectrometer with 1.8 T electromagnet and Stinger closed-cycle helium gas cryostat. Powders of **1-Ce**, **1-Nd** and **1-U** were finely ground in a glovebox, and 1-2 cm of each sample was loaded into to a 4 mm outer diameter (OD) quartz tube and sealed under vacuum. A solution of **1-Nd** in 2-Me-THF (15 mM) was prepared in a glovebox. Quartz tubes of OD 4 mm were filled with ~3 cm of solution, which was immediately frozen and flame-sealed under vacuum, and then rapidly transferred to the spectrometer within *ca.* 15 mins. Spectra were obtained at base temperature (4-7 K) and powder spectra were obtained for two rotations at ~90 degrees to one another to identify any features due to polycrystallinity. The field was corrected using a strong pitch sample (g = 2.0028). Spectra were simulated in EasySpin 6.0.0-dev.51.[64] Powder spectra of **1-Ce** and **1-Nd** were simulated in the EasySpin function pepper as an effective $S = ½$, with rhombic g values, $g = [g_1, g_2, g_3]$ and gStrains (distribution of g values) to account for all line broadenings effects. For **1-Nd**, g_3 was not observed (< 0.4) and so was fixed to 0.2. Hyperfine coupling on the g_1 feature (A_1) for **1-Nd** was included for the most abundant isotope and scaled for other isotopes based on nuclear g-factors.

The H-only structural optimization of diamagnetic **1-La**, and full geometry optimization of desolvated $La(THF)_1$ and $La(THF)_0$ analogues were performed using ADF 2017;[65-67] structural optimization of paramagnetic **1-M** (where performed) and desolvated $M(THF)_1$ and $M(THF)_0$ analogues were conducted in the gas phase using DFT with Gaussian 16[106] and electron correlation were described using the PBE functional.[107] All central lanthanide atoms were treated with the Stuttgart RSC-ANO ECP basis set,[108-110] and all remaining atoms with cc-pVDZ.[111] Diamagnetic NMR chemical shifts were computed with ADF 2017.[65-67] Spin-orbit relativistic, single-point calculations, using the optimized geometries described above, employed either the BP86, PBE0, SAOP or B3LYPHFXX (XX = 10, 15, 20, 25, 30, 35, 40, 45, 50) hybrid functionals. All-electron Slater-type orbital triple-ζ quality basis sets (TZ2P) were employed in conjunction with the two-component zero-order regular approximation (ZORA) Hamiltonian.[112-114] The ^{29}Si NMR chemical shifts are reported relative to TMS. Scalar relativistic approaches (spin-orbit neglected) were used within the ZORA Hamiltonian to include relativistic effects,[112,113,115] and a benzene solvent continuum was added. The local density approximation (LDA) with a correlation potential was used in all calculations.[116] Generalized gradient approximation corrections were performed using the functionals of Becke and Perdew.[117,118] NBO analysis was carried out using NBO6.[82] QTAIM analysis[83,84] was performed within the ADF package; the MOs and NBOs were visualized using ADFView.[66,67]

CASSCF-SO calculations were performed with OpenMolcas[77] on XRD structures of paramagnetic **1-M**. Basis sets from the ANO-RCC library[119-121] were used with VTZP quality on the metal atom, VDZP quality on the coordinating atoms and VDZ quality on all other atoms, employing the second-order DKH transformation. Cholesky decomposition of the two-electron integrals with a threshold of 10^{-8} was performed to save disk space and reduce computational demand. The molecular orbitals (MOs) were averaged in state-averaged CASSCF calculations with active spaces of (1,7) (**1-Ce**), (2,7) (**1-Pr**) and (3,7) (**1-Nd** and **1-U**) averaging over seven doublets (**1-Ce**), 21 triplets and 28 singlets (**1-Pr**), and 35 quartets and 112 doublets (**1-Nd** and **1-U**). The spin-free wavefunctions obtained from these CASSCF calculations were mixed by spin-orbit coupling in the RASSI module. The *g*-values, magnetization and magnetic susceptibility (isotropic value and tensor) were calculated using SINGLE_ANISO,[122] and the spin-orbit wavefunctions were decomposed into their crystal field wavefunctions, with the quantization axis defined by the g_1 direction in the ground doublet. From the magnetic susceptibility tensor we calculate the pseudo-contact shift ($\delta_{\mathrm{PCS}}^{\mathrm{para}}$) for the ^{29}Si and ^{1}H nuclei as:

$$\delta_{\mathrm{pc}} = \frac{1}{4\pi r^3}\left[(\chi_{zz} - \bar{\chi})\frac{2z^2-x^2-y^2}{2r^2} + (\chi_{xx} - \chi_{yy})\frac{x^2-y^2}{2r^2} + \chi_{xy}\frac{2xy}{r^2} + \chi_{xz}\frac{2xz}{r^2} + \chi_{yz}\frac{2yz}{r^2}\right]$$

where $\bar{\chi} = \frac{1}{3}\mathrm{Tr}(\boldsymbol{\chi})$.[89] To calculate $\delta_{\mathrm{PCS}}^{\mathrm{para}}$ we have implemented the paramagnetic component of the van den Heuvel and Soncini method[47] in our HYPERION code,[123] which uses a full sum-over-states expression derived from the derivative of the Helmholtz free energy:

$$\sigma_{ij}^{para} = \frac{1}{\mathcal{Q}_0}\sum_n e^{-\beta E_n}\left[\begin{array}{c}\beta\sum_{v,v'}\langle n\,v|\hat{m}_i|n\,v'\rangle\langle n\,v'|\hat{\mathcal{F}}_j|n\,v\rangle \\ +\sum_{m\neq n}\sum_{v,\mu}\frac{\langle n\,v|\hat{m}_i|m\,\mu\rangle\langle m\,\mu|\hat{\mathcal{F}}_j|n\,v\rangle + c.c.}{E_m - E_n}\end{array}\right]$$

where the paramagnetic shielding tensor σ_{ij}^{para} is related to the paramagnetic shift by $\delta_{\mathrm{vdH-S}}^{\mathrm{para}} = -\frac{1}{3}Tr(\boldsymbol{\sigma}^{para})$, $\hat{m}$ and $\hat{\mathcal{F}}$ are the Zeeman and hyperfine operators respectively, and n and m are levels with degenerate states v, μ respectively.

General procedure for the synthesis of 1-M. A Schlenk flask was charged with [$MI_3(THF)_x$] (M = La, Ce, Pr, U, x = 4; M = Nd, x = 3.5) and diethyl ether (20 mL/ mmol) and was cooled to –78 °C. [K{$Si(SiMe_3)_3$}] (3 eq.) was dissolved in diethyl ether (5 mL/mmol) in another Schlenk flask and was added dropwise to the cooled [$MI_3(THF)_x$] suspension with stirring. The yellow reaction mixture was stirred for 1 hr at –78 °C, then allowed to warm to room temperature. During this time, the color of the reaction mixture either remained yellow (M = La) or darkened to orange (M = Ce, Pr), brown (M = Nd) or dark green (M = U). After reaching room temperature all volatiles were immediately removed *in vacuo* and

the product was extracted with hexane (40 mL/mmol). Concentration and storage of the filtrate at –25 °C led to the formation of needles of [M{Si(SiMe$_3$)$_3$}$_3$(THF)$_2$] (**1-M**).

[La{Si(SiMe$_3$)$_3$}$_3$(THF)$_2$] (1-La). Prepared according to the general procedure with [LaI$_3$(THF)$_4$] (0.744 g, 1 mmol) and [K{Si(SiMe$_3$)$_3$}] (0.860 g, 3 mmol); **1-La** was obtained as yellow needles (0.425 g, 0.41 mmol, 41%). Anal. Calcd for $C_{35}H_{97}LaO_2Si_{12}$: C, 40.97; H, 9.53. Found: C, 39.99; H, 9.83. ^{1}H NMR (C_6D_6/C_4D_8O (9:1), 400 MHz): δ 3.62 (OC*H*$_2$CH$_2$), 1.46 (OCH$_2$C*H*$_2$), 0.41 (s, 54H, Si(C*H*$_3$)$_3$ group 2), 0.23 (s, 27H, Si(C*H*$_3$)$_3$ group 1). ^{13}C{^{1}H} NMR (C_6D_6/C_4D_8O (9:1), 101 MHz): δ 68.18 (O*C*H$_2$CH$_2$), 25.80 (OCH$_2$*C*H$_2$), 6.78 (Si(*C*H$_3$)$_3$ group 2), 1.39 (Si(*C*H$_3$)$_3$ group 1). ^{29}Si{^{1}H} NMR (C_6D_6/C_4D_8O (9:1), 79 MHz): δ –5.3 (*Si*Me$_3$ group 2), –13.1 (*Si*Me$_3$ group 1), –82.3 (La*Si*). ATR-IR (microcrystalline, cm^{-1}) $\tilde{\nu}$: 2945 (m), 2891 (m), 1237 (s), 1004 (w), 820 (s), 743 (w), 676 (m), 622 (m), 421 (m). UV-Vis-NIR (2 mM in THF, cm^{-1}) $\tilde{\upsilon}_{max}$: 27,150 (ε = 1760 M^{-1} cm^{-1}).

[Ce{Si(SiMe$_3$)$_3$}$_3$(THF)$_2$] (1-Ce). Prepared according to the general procedure with [CeI$_3$(THF)$_4$] (0.745 g, 1 mmol) and [K{Si(SiMe$_3$)$_3$}] (0.860 g, 3 mmol); **1-Ce** was obtained as orange needles (0.425 g, 0.41 mmol, 41%). Anal. Calcd for $C_{35}H_{97}CeO_2Si_{12}$: C, 40.92; H, 9.52. Found: C, 37.01; H, 9.02. ^{1}H NMR (C_6D_6/C_4D_8O (9:1), 400 MHz): δ 3.74 (OC*H*$_2$CH$_2$), 1.55 (s, 27H, Si(C*H*$_3$)$_3$ group 1), 1.51 (OCH$_2$C*H*$_2$), –1.43 (s, 54H, Si(C*H*$_3$)$_3$ group 2). ^{13}C{^{1}H} NMR (C_6D_6/C_4D_8O (9:1), 101 MHz): δ 68.18 (O*C*H$_2$CH$_2$), 25.95 (OCH$_2$*C*H$_2$), 6.30 (Si(*C*H$_3$)$_3$ group 2), 2.78 (Si(*C*H$_3$)$_3$ group 1). ^{29}Si{^{1}H} NMR (C_6D_6/C_4D_8O (9:1), 79 MHz): δ –6.4 (*Si*Me$_3$ group 2), –11.4 (*Si*Me$_3$ group 1), –79.4 (Ce*Si*). ATR-IR (microcrystalline, cm^{-1}) $\tilde{\nu}$: 2945 (m), 2891 (m), 1237 (s), 1004 (w), 820 (s), 743 (w), 676 (m), 622 (m), 421 (m). UV-Vis-NIR (2 mM in THF, cm^{-1}) $\tilde{\upsilon}_{max}$: 26,750 (ε = 1010 M^{-1} cm^{-1}), 23,300 (ε = 240 M^{-1} cm^{-1}).

[Pr{Si(SiMe$_3$)$_3$}$_3$(THF)$_2$] (1-Pr). Prepared according to the general procedure with [PrI$_3$(THF)$_4$] (0.747 g, 1 mmol) and [K{Si(SiMe$_3$)$_3$}] (0.860 g, 3 mmol); **1-Pr** was obtained as yellow needles (0.362 g, 0.35 mmol, 35%). Anal. Calcd for $C_{35}H_{97}PrO_2Si_{12}$: C, 40.89; H, 9.51. Found: C, 36.84; H, 9.18. ^{1}H NMR (C_6D_6/C_4D_8O (9:1), 400 MHz): δ 8.13 (s, 27H, Si(C*H*$_3$)$_3$ group 1), –7.66 (s, 54H, Si(C*H*$_3$)$_3$ group 2), OC*H*$_2$CH$_2$ and OCH$_2$C*H*$_2$ signals not observed. ^{13}C{^{1}H} NMR (C_6D_6/C_4D_8O (9:1), 101 MHz): δ 9.74 (Si(*C*H$_3$)$_3$, group 1), O*C*H$_2$CH$_2$, OCH$_2$*C*H$_2$ and Si(*C*H$_3$)$_3$ group 2 signals not observed. ^{29}Si{^{1}H} NMR (C_6D_6/C_4D_8O (9:1), 79 MHz): δ –2.9 (*Si*Me$_3$, group 1), –65.5 (Pr*Si*), *Si*(CH$_3$)$_3$ group 2 signals not observed. ATR-IR (microcrystalline, cm^{-1}) $\tilde{\nu}$: 2945 (m), 2891 (m), 1237 (s), 1004 (w), 820 (s), 743 (w), 676 (m), 622 (m), 421 (m). UV-Vis-NIR (2 mM in THF, cm^{-1}) $\tilde{\upsilon}_{max}$: no transitions observed, tail from 22,200 cm^{-1}.

[Nd{Si(SiMe$_3$)$_3$}$_3$(THF)$_2$] (1-Nd). Prepared according to the general procedure with [NdI$_3$(THF)$_{3.5}$] (0.721 g, 1 mmol) and [K{Si(SiMe$_3$)$_3$}] (0.860 g, 3 mmol); **1-Nd** was obtained as red needles (0.336 g, 0.33 mmol, 33%). Anal. Calcd for $C_{35}H_{97}NdO_2Si_{12}$: C, 40.76; H, 9.48. Found: C, 38.42; H, 9.46. ^{1}H NMR (C_6D_6/C_4D_8O (9:1), 400 MHz): δ 5.08

(s, 27H, Si(CH_3)$_3$ group 1), –4.63 (br, s, FWHM = 69.5 Hz, 54H, Si(CH_3)$_3$ group 2), OCH_2CH$_2$ and OCH$_2$CH_2 signals not observed. ^{13}C{^{1}H} NMR (C_6D_6/C_4D_8O (9:1), 101 MHz): δ 6.51 (Si(*C*H$_3$)$_3$, group 1), O*C*H$_2$CH$_2$, OCH$_2$*C*H$_2$ and Si(*C*H$_3$)$_3$ group 2 signals not observed. ^{29}Si{^{1}H} NMR (C_6D_6/C_4D_8O (9:1), 79 MHz): δ –6.8 (*Si*Me$_3$, group 1), –71.6 (Nd*Si*), *Si*(CH$_3$)$_3$ group 2 signals not observed. ATR-IR (microcrystalline, cm^{-1}) $\tilde{\nu}$: 2945 (m), 2891 (m), 1237 (s), 1004 (w), 820 (s), 743 (w), 676 (m), 622 (m), 421 (m). UV-Vis-NIR (2 mM in THF, cm^{-1}) $\tilde{\upsilon}_{max}$: 17,250 (ε = 30 M^{-1} cm^{-1}, $^4I_{9/2}$ → $^4G_{5/2}$).

[U{Si(SiMe$_3$)$_3$}$_3$(THF)$_2$] (1-U). Prepared according to the general procedure with [UI$_3$(THF)$_4$] (0.843 g, 1 mmol) and [K{Si(SiMe$_3$)$_3$}] (0.860 g, 3 mmol); **1-U** was obtained as dark green needles (0.569 g, 0.51 mmol, 51%). Anal. Calcd for $C_{35}H_{97}UO_2Si_{12}$: C, 37.36; H, 8.69. Found: C, 35.48; H, 8.59. ^{1}H NMR (C_6D_6/C_4D_8O (9:1), 400 MHz): δ 5.63 (s, 27H, Si(CH_3)$_3$ group 1), 4.24 (OCH_2CH$_2$), 1.75 (OCH$_2$CH_2), –6.84 (br, s, FWHM = 65.4 Hz, 54H, Si(CH_3)$_3$ group 2). ^{13}C{^{1}H} NMR (C_6D_6/C_4D_8O (9:1), 101 MHz): δ 25.71 (OCH$_2$*C*H$_2$), 7.05 (Si(*C*H$_3$)$_3$, group 1), OCH$_2$*C*H$_2$ and Si(*C*H$_3$)$_3$ group 2 signals not observed. ^{29}Si{^{1}H} NMR (C_6D_6/C_4D_8O (9:1), 79 MHz): δ –6.0 (*Si*Me$_3$, group 1), –70.5 (U*Si*), *Si*(CH$_3$)$_3$ group 2 signals not observed. ATR-IR (microcrystalline, cm^{-1}) $\tilde{\nu}$: 2945 (m), 2891 (m), 1237 (s), 1004 (w), 820 (s), 743 (w), 676 (m), 622 (m), 421 (m). UV-Vis-NIR (2 mM in THF, cm^{-1}) $\tilde{\upsilon}_{max}$: 20,500 (ε = 1420 M^{-1} cm^{-1}), 19,500 (ε = 1150 M^{-1} cm^{-1}), 18,000 (ε = 1190 M^{-1} cm^{-1}), 17,100 (ε = 1050 M^{-1} cm^{-1}), 16,200 (ε = 930 M^{-1} cm^{-1}), 15,700 (ε = 830 M^{-1} cm^{-1}), 13,650 (ε = 790 M^{-1} cm^{-1}), 12,750 (ε = 560 M^{-1} cm^{-1}), 12,000 (ε = 380 M^{-1} cm^{-1}), 11,250 (ε = 250 M^{-1} cm^{-1}), 10,050 (ε = 90 M^{-1} cm^{-1}), 9,500 (ε = 80 M^{-1} cm^{-1}), 8,650 (ε = 120 M^{-1} cm^{-1}).

Associated Content

Supporting Information

Additional experimental details, materials, methods, and data associated with this manuscript are compiled in the Supporting Information.

Additional Information

Research data files supporting this publication are available from FigShare at https://figshare.com/10.6084/m9.figshare.25288882.

Accession Codes

CCDC 2329788–2329792 contain the supplementary crystallographic data for this paper. These data can be obtained free of charge via www.ccdc.cam.ac.uk/data_request/cif, or by emailing data_request@ccdc.cam.ac.uk, or by contacting The Cambridge Crystallographic Data Centre, 12 Union Road, Cambridge, CB2 1EZ, UK; fax: +44 1223 336033.

Notes

The authors declare no competing financial interest.

Acknowledgements

We thank the University of Manchester for a PhD studentship for B.L.L.R. (Nuclear Endowment) and access to the Computational Shared Facility, and the Engineering and Physical Sciences Research Council (EPSRC) (EP/P001386/1, EP/V007580/1, EP/W021463/1, and EP/M027015/1) and European Research Council (StG-851504, CoG-816268 and CoG-612724) for funding. We thank the EPSRC UK National Electron Paramagnetic Resonance Service for access to the EPR facility and SQUID magnetometer (EP/S033181/1). S.T.L. thanks the Alexander von Humboldt Foundation for a Friedrich Wilhelm Bessel Research Award, N.F.C. thanks the Royal Society for a University Research Fellowship (URF191320) and The Australian National University for an ANU Futures grant, and B. Alnami thanks Kuwait University for a PhD scholarship. We thank Ralph Adams for support of solution NMR experiments.

Author contributions

B.L.L.R., S.T.L. and D.P.M. provided the original concept. B.L.L.R. and F.J.M. synthesized and characterized the compounds and solved and refined the single crystal XRD data. G.K.G. collected and interpreted EPR and magnetic data and performed *ab initio* calculations. B. Atkinson implemented new pNMR code. B. Alnami performed pNMR calculations and analysis. S.T.L. performed the diamagnetic NMR calculations. C.A.M. and J.B. carried out supporting synthetic and characterization work. D.B. and D.L. collected, interpreted, and modelled solid-state NMR spectra. A.J.W. further refined the single crystal XRD data and finalized CIFs. I.J.V.Y. collected, solved, refined and modelled powder XRD data. N.F.C. supervised the EPR spectroscopy, magnetism, and calculations components. D.L. supervised the solid-state NMR spectroscopy component. D.P.M. and S.T.L. supervised the synthetic component and directed the research. B.L.L.R., B. Alnami, D.L., N.F.C., S.T.L. and D.P.M. wrote the manuscript, with contributions from all authors.

References

1. *The Lanthanides and Actinides*, Liddle, S. T.; Mills, D. P.; Natrajan, L. S. Eds. World Scientific Publishing Europe Ltd.: Singapore, 2022.

2. Aspinall, H. C. Chiral Lanthanide Complexes: Coordination Chemistry and Applications. *Chem. Rev.* **2002**, *102* (6), 1807–1850.

3. Clark, R. L.; Wenzel, B. T.; Wenzel, T. J. Diamagnetic lanthanide tris β-diketonate complexes with aryl-containing ligands as chiral NMR discriminating agents. *Tetrahedron: Asymmetry* **2013**, *24* (5-6), 297–304.

4. Wenzel, T. J.; Patton, W. R. Chapter 10. Advances in the use of lanthanide enolates as nuclear magnetic resonance shift reagents, in *The Chemistry of Metal Enolates, Volume 2*, Zabicky, J. Ed. in *Patai's Chemistry of Functional Groups*, Rappoport, Z. Ed.; John Wiley & Sons, Ltd., Chichester, 2018; pp. 399–420.

5. Finney, K.-L. N. A.; Harnden, A. C.; Rogers, N. J.; Senanayake, P. K.; Blamire, A. M.; O'Hogain, D.; Parker, D. Simultaneous Triple Imaging with Two PARASHIFT Probes: Encoding Anatomical, pH and Temperature Information using Magnetic Resonance Shift Imaging. *Chem. Eur. J.* **2017**, *23* (33), 7976–7989.

6. Senanayake, P. K.; Rogers, N. J.; Finney, K.-L. N. A.; Harvey, P.; Funk, A. M.; Wilson, J. I.; O'Hogain, D.; Maxwell, R.; Parker, D.; Blamire, A. M. A new paramagnetically shifted imaging probe for MRI. *Magn. Reson. Med.* **2017**, *77* (3), 1307–1317.

7. Harnden, A. C.; Parker, D.; Rogers, N. J. Employing paramagnetic shift for responsive MRI probes. *Coord. Chem. Rev.* **2019**, *383*, 30–42.

8. Butler, S. J.; Delbianco, M.; Lamarque, L.; McMahon, B. K.; Neil, E. R.; Pal, R.; Parker, D.; Walton, J. W.; Zwier, J. M. EuroTracker® dyes: design, synthesis, structure and photophysical properties of very bright europium complexes and their use in bioassays and cellular optical imaging. *Dalton Trans.* **2015**, *44*, 4791–4803.

9. Delbianco, M.; Sadovnikova, V.; Bourrier, E.; Mathis, G.; Lamarque, L.; Zwier, J. M.; Parker, D. Bright, Highly Water-Soluble Triazacyclononane Europium Complexes To Detect Ligand Binding with Time-Resolved FRET Microscopy. *Angew. Chem. Int. Ed.* **2014**, *53* (40), 10718–10722.

10. Shuvaev, S.; Starck, M.; Parker, D. Responsive, Water-Soluble Europium(III) Luminescent Probes. *Chem. Eur. J.* **2017**, *23* (42), 9974–9989.

11. Müntener, T.; Kottelat, J.; Huber, A.; Häussinger, D. New Lanthanide Chelating Tags for PCS NMR Spectroscopy with Reduction Stable, Rigid Linkers for Fast and Irreversible Conjugation to Proteins. *Bioconjugate Chem.* **2018**, *29* (10), 3344–3351.

12. Nitsche, C.; Otting, G. Pseudocontact shifts in biomolecular NMR using paramagnetic metal tags. *Prog. Nucl. Magn. Reson. Spectrosc.* **2017**, *98–99*, 20–49.

13. Pan, B.-B.; Yang, F.; Ye, Y.; Wu, Q.; Li, C.; Huber, T.; Su, X.-C. 3D structure determination of a protein in living cells using paramagnetic NMR spectroscopy. *Chem. Commun.* **2016**, *52*, 10237–10240.

14. Suturina, E. A.; Kuprov, I. Pseudocontact shifts from mobile spin labels. *Phys. Chem. Chem. Phys.* **2016**, *18*, 26412–26422.

15. Lee, M. D.; Dennis, M. L.; Swarbrick, J. D.; Graham, B. Enantiomeric two-armed lanthanide-binding tags for complementary effects in paramagnetic NMR spectroscopy. *Chem. Commun.* **2016**, *52*, 7954–7957.

16. Ravera, E.; Parigi, G.; Luchinat, C. Perspectives on paramagnetic NMR from a life sciences infrastructure. *J. Magn. Reson.* **2017**, *282*, 154–169.

17. Dietel, A. M.; Tok, O.; Kempe, R. f-Block-Element–f-Block-Element NMR Spin–Spin Coupling. *Eur. J. Inorg. Chem.* **2007**, 4583–4586.

18. Dietel, A. M.; Döring, C.; Glatz, G.; Butovskii, M. V.; Tok, O.; Schappacher, F. M.; Pöttgen, R.; Kempe, R. Bimetallic Complexes of Ytterbium and Europium Stabilized by Sterically Demanding Dipyridylamides. *Eur. J. Inorg. Chem.* **2009**, 1051–1059.

19. Vícha, J.; Novotný, J.; Komorovsky, S.; Straka, M.; Kaupp, M.; Marek, R. Relativistic Heavy-Neighbor-Atom Effects on NMR Shifts: Concepts and Trends across the Periodic Table. *Chem. Rev*. **2020**, *120* (15), 7065–7103.

20. Iggo, J. A.; Luzyanin, K. *NMR Spectroscopy in Inorganic Chemistry*, Second Edition; Oxford University Press, Oxford, 2020.

21. Parker, D.; Suturina, E. A.; Kuprov, I.; Chilton, N. F. How the Ligand Field in Lanthanide Coordination Complexes Determines Magnetic Susceptibility Anisotropy, Paramagnetic NMR Shift, and Relaxation Behavior. *Acc. Chem. Res.* **2020**, *53* (8), 1520–1534.

22. Autillo, M.; Guerin, L.; Bolvin, H.; Moisy, P.; Berthon, C. Magnetic susceptibility of actinide(iii) cations: an experimental and theoretical study. *Phys. Chem. Chem. Phys.* **2016**, *18*, 6515–6525.

23. Pell, A. J.; Pintacuda, G.; Grey, C. P. Paramagnetic NMR in solution and the solid state. *Prog. Nucl. Magn. Reson. Spectrosc.* **2019**, *111*, 1–271.

24. Fusaro, L.; Casella, G.; Bagno, A. Direct Detection of ^{17}O in $[Gd(DOTA)]^-$ by NMR Spectroscopy. *Chem. Eur. J.* **2015**, *21*, 1955–1920.

25. Edelmann, F. T.; Freckmann, D. M. M.; Schumann, H. Synthesis and Structural Chemistry of Non-Cyclopentadienyl Organolanthanide Complexes. *Chem. Rev.* **2002**, *102* (6), 1851–1896.

26. Zimmermann, M.; Anwander, R. Homoleptic Rare-Earth Metal Complexes Containing Ln−C σ-Bonds. *Chem. Rev.* **2010**, *110* (10), 6194–6259.

27. Reánt, B. L. L.; Liddle, S. T.; Mills, D. P. f-Element Silicon and Heavy Tetrel Chemistry. *Chem. Sci.* **2020**, *11* (40), 10871–10886.

28. Castillo, I.; Tilley, T. D. Organolutetium Complexes in σ-Bond Metathesis Reactions Involving Silicon. Catalysts for the Hydrogenolysis of Si−C Bonds. *Organometallics* **2001**, *20* (26), 5598–5605.

29. Sadow, A. D.; Tilley, T. D. Synthesis and Characterization of Scandium Silyl Complexes of the Type $Cp^*_2ScSiHRR'$. σ-Bond Metathesis Reactions and Catalytic Dehydrogenative Silation of Hydrocarbons. *J. Am. Chem. Soc.* **2005**, *127* (2), 643–656.

30. Pan, F.; Zhang, J.; Chen, H. L.; Su, Y. H.; Kuo, C. L.; Su, Y. H.; Chen, S. H.; Lin, K. J.; Hsieh, P. H.; Hwang, W. S. Effects of Rare Earth Metals on Steel Microstructures. *Materials* **2016**, *9* (6), 417.

31. White, J. T.; Nelson, A. T.; Dunwoody, J. T.; Byler, D. D.; Safarik, D. J.; McClellan, K. J. Thermophysical properties of U_3Si_2 to 1773 K. *J. Nucl. Mater.* **2015**, *464*, 275–280.

32. Wilson, T. L.; Moore, E. E.; Adorno Lopes, D.; Kocevski, V.; Sooby Wood, E.; White, J. T.; Nelson, A. T.; McMurray, J. W.; Middleburg, S. C.; Xu, P.; Besmann, T. M. Uranium nitride-silicide advanced nuclear fuel: higher efficiency and greater safety. *Adv. Appl. Ceram.* **2018**, *117*, s76–s81.

33. Humphrey, U. E.; Khandaker, M. U. Viability of thorium-based nuclear fuel cycle for the next generation nuclear reactor: Issues and prospects. *Renew. Sustain. Energy Rev.* **2018**, *97*, 259–275.

34. He, S.; J. Cai, J. The potentiality of thermal safety and economy of the U_3Si_2-SiC system in PWR. *Ann. Nucl. Energy* **2020**, *140*, 107303.

35. Marschner, C. Oligosilanes. In *Functional Molecular Silicon Compounds I*; Scheschkewitz, D. Ed. Springer Verlag, 2014; Vol. 155, pp 163–228.

36. Zitz, R.; Hlina, J.; Gatterer, K.; Marschner, C.; Szilvási, T.; Baumgartner, J. Neutral “Cp-Free” Silyl-Lanthanide(II) Complexes: Synthesis, Structure, and Bonding Analysis. *Inorg. Chem.* **2015**, *54* (14), 7065–7072.

37. Corradi, M. M.; Frankland, A. D.; Hitchcock, P. B.; Lappert, M. F.; Lawless, G. A. Synthesis, structure and reactivity of $[Yb(\eta\text{-}C_5Me_5)\{Si(SiMe_3)_3\}(thf)_2]$. *Chem. Commun.* **1996**, 2323–2324.

38. Sgro, M. J.; Piers, W. E. Synthesis, Characterization and Reactivity of Yttrium and Gadolinium Silyl Complexes. *Inorg. Chim. Acta* **2014**, *422*, 243–250.

39. Campion, B. K.; Heyn, R. H.; Tilley, T. D. Synthesis and reactions of silyl and germyl derivatives of scandocene. Structure of $Cp_2Sc[Si(SiMe_3)_3](THF)$. *Organometallics* **1993**, *12* (7), 2584–2590.

40. Zitz, R.; Hlina, J.; Arp, H.; Kinschel, D.; Marschner, C.; Baumgartner, J. Group 4 Metal and Lanthanide Complexes in the Oxidation State +3 with Tris(trimethylsilyl)silyl Ligands. *Inorg. Chem.* **2019**, *58* (10), 7107–7117.

41. Gransbury, G. K.; Réant, B. L. L.; Wooles, A. J.; Emerson-King, J.; Chilton, N. F.; Liddle, S. T.; Mills, D. P. Electronic structure comparisons of isostructural early d- and f-block metal(III) bis(cyclopentadienyl) silanide complexes. *Chem. Sci.* **2023**, *14* (3), 621–634.

42. Réant, B. L. L.; Wooles, A. J.; Liddle, S. T.; Mills, D. P. Synthesis and Characterization of Yttrium Methanediide Silanide Complexes. *Inorg. Chem.* **2023**, *62* (1), 137–146.

43. Diaconescu, P. L.; Odom, A. L.; Agapie, T.; Cummins, C. C. Uranium−Group 14 Element Single Bonds: Isolation and Characterization of a Uranium(IV) Silyl Species. *Organometallics* **2001**, *20* (24), 4993–4995.

44. Reánt, B. L. L.; Berryman, V. E. J.; Seed, J. A.; Basford, A. R.; Formanuik, A.; Wooles, A. J.; Kaltsoyannis, N.; Liddle, S. T.; Mills, D. P. Polarised Covalent Thorium(IV)- and Uranium(IV)-Silicon Bonds. *Chem. Commun.* **2020**, *56* (83), 12620–12623.

45. Lin. N. J.; Zeller, M.; Bart, S. C. Solution and solid-state characterization of rare silyluranium(III) complexes. *Chem. Commun*. **2024**, *60*, 3954–3957.

46. Réant, B. L. L.; Berryman, V. E. J.; Basford, A. R.; Nodaraki, L. E.; Wooles, A. J.; Tuna, F.; Kaltsoyannis, N.; Mills, D. P.; Liddle, S. T. ^{29}Si NMR Spectroscopy as a Probe of s- and f-Block Metal(II)-Silanide Bond Covalency. *J. Am. Chem. Soc.* **2021**, *143* (26), 9813–9824.

47. van den Heuvel, W.; Soncini, A. NMR chemical shift as analytical derivative of the Helmholtz free energy. *J. Chem. Phys.* **2013**, *138*, 054113.

48. Hitchcock, P. B.; Lappert, M. F.; Maron, L.; Protchenko, A. V. Lanthanum Does Form Stable Molecular Compounds in the +2 Oxidation State. *Angew. Chem. Int. Ed.* **2008**, *47*, 1488–1491.

49. Kuveke, R. E. H.; Barwise, L.; van Ingen, Y.; Vashisth, K.; Roberts, N.; Chitnis, S. S.; Dutton, J. L.; Marti, C. D.; Melen, R. L. An International Study Evaluating Elemental Analysis. *ACS Cent. Sci.* **2022**, *8*, 855–863.

50. Addison, A. W.; Rao, T. N.; Reedijk, J.; Van Rijn, J.; Verschoor, G. C. Synthesis, structure, and spectroscopic properties of copper(II) compounds containing nitrogen–sulphur donor ligands; the crystal and molecular structure of

aqua[1,7-bis(*N*-methylbenzimidazol-2′-yl)-2,6-dithiaheptane]copper(II) perchlorate. *J. Chem. Soc. Dalton Trans.* **1984**, *7*, 1349–1356.

51. Shannon, R. D. Revised Effective Ionic Radii and Systematic Studies of Interatomic Distances in Halides and Chalcogenides. *Acta Crystallogr. Sect. A* **1976**, *32*, 751–767.

52. Pyykkö, P. Additive Covalent Radii for Single-, Double-, and Triple-Bonded Molecules and Tetrahedrally Bonded Crystals: A Summary. *J. Phys. Chem. A* **2015**, *119* (11), 2326–2337.

53. Kyushin, S.; Sakurai, H.; Matsumoto, H. Highly Planar Silane $[(i\text{-}Pr)_3Si]_3SiH$ and Silyl Radical $[(i\text{-}Pr)_3Si]_3Si\cdot$. *Chem. Lett.* **1998**, *27* (2), 107–108.

54. Marschner, C. A New and Easy Route to Polysilanylpotassium Compounds. *Eur. J. Inorg. Chem.* **1998**, 221–226.

55. Pan, X.; Wu, C.; Fang, H.; Yan, C. Early Lanthanide(III) Ate Complexes Featuring Ln-Si Bonds (Ln = La, Ce): Synthesis, Structural Characterization, and Bonding Analysis. *Inorg. Chem.* **2022**, *61* (36), 14288–14296.

56. Braunschweig, H.; Colling, M.; Kollann, C.; Merz, K.; Radacki, K. $[(OC)_5Cr{=}BSi(SiMe_3)_3]$: A Terminal Borylene Complex with an Electronically Unsaturated Boron Atom. *Angew. Chem. Int. Ed.* **2001**, *40* (22), 4198–4200.

57. Volkovich, V. A.; Ivanov, A. B.; Yakimov, S. M.; Tsarevskii, D. V.; Golovanova, O. A.; Sukhikh, V. V.; Griffiths, T. R. Electronic absorption spectra of rare earth (III) species in NaCl–2CsCl eutectic based melts. *AIP Conf. Proc.* **2016**, *1767*, 020023.

58. Liddle, S. T. The Renaissance of Non-Aqueous Uranium Chemistry. *Angew. Chem. Int. Ed.* **2015**, *54* (30), 8604–8641.

59. Morris, D. E.; Da Re, R. E.; Jantunen, K. C.; Castro-Rodriguez, I.; Kiplinger, J. L. Trends in Electronic Structure and Redox Energetics for Early-Actinide Pentamethylcyclopentadienyl Complexes. *Organometallics* **2004**, *23* (22), 5142–5153.

60. Graves, C. R.; Yang, P.; Kozimor, S. A.; Vaughn, A. E.; Clark, D. L.; Conradson, S. D.; Schelter, E. L.; Scott, B. J.; Thompson, J. D.; Hay, P. J.; Morris, D. E.; Kiplinger, J. L. Organometallic Uranium(V)−Imido Halide Complexes: From Synthesis to Electronic Structure and Bonding. *J. Am. Chem. Soc.* **2008**, *130* (15), 5272–5285.

61. Mills, D. P.; Moro, F.; McMaster, J.; van Slageren, J.; Lewis, W.; Blake, A. J.; Liddle, S. T. A delocalized arene-bridged diuranium single-molecule magnet. *Nat. Chem.* **2011**, *3*, 454–460.

62. Wooles, A. J.; Mills, D. P.; Tuna, F.; McInnes, E. J. L.; Law, G. T. W.; Fuller, A. J.; Kremer, F.; Ridgway, M.; Lewis, W.; Gagliardi, L.; Vlaisavljevich, B.; Liddle, S. T. Uranium(III) Carbon Multiple Bonding Supported by Arene δ-Bonding in Mixed Valence Hexauranium Nanometre-Scale Rings. *Nat. Commun.* **2018**, *9*, 2097.

63. Brackbill, I. J.; Douair, I.; Lussier, D. J.; Boreen, M. A.; Maron, L.; Arnold, J. Synthesis and Structure of Uranium-Silylene Complexes. *Chem. Eur. J.* **2020**, *26* (11), 2360–2364.

64. Stoll, S.; Schweiger, A. EasySpin, a Comprehensive Software Package for Spectral Simulation and Analysis in EPR. *J. Magn. Reson.* **2006**, *178* (1), 42–55.

65. *ADF SCM*; Theoretical Chemistry, Vrije Universiteit: Amsterdam, The Netherlands, 2017.

66. Fonseca Guerra, C.; Snijders, J. G.; Te Velde, G.; Baerends, E. J. Towards an Order-N DFT Method. *Theor. Chem. Acc.* **1998**, *99* (6), 391–403.

67. Velde, G. Te; Bickelhaupt, F. M.; Baerends, E. J.; Fonseca Guerra, C.; van Gisbergen, S. J. A.; Snijders, J. G.; Ziegler, T. Chemistry with ADF. *J. Comput. Chem.* **2001**, *22* (9), 931–967.

68. Ernzerhof, M.; Scuseria, G. E. Assessment of the Perdew-Burke-Ernzerhof Exchange-Correlation Functional. *J. Chem. Phys.* **1999**, *110* (11), 5029–5036.

69. Hrobárik, P.; Hrobáriková, V.; Greif, A. H.; Kaupp, M. Giant Spin-Orbit Effects on NMR Shifts in Diamagnetic Actinide Complexes: Guiding the Search of Uranium(VI) Hydride Complexes in the Correct Spectral Range. *Angew. Chem. Int. Ed.* **2012**, *51* (43), 10884–10888.

70. Seaman, L. A.; Hrobárik, P.; Schettini, M. F.; Fortier, S.; Kaupp, M.; Hayton, T. W. A Rare Uranyl(VI)-Alkyl Ate Complex $[Li(DME)_{1.5}]_2[UO_2(CH_2SiMe_3)_4]$ and Its Comparison with a Homoleptic Uranium(VI)-Hexaalkyl. *Angew. Chem. Int. Ed.* **2013**, *52* (11), 3259–3263.

71. Smiles, D. E.; Wu, G.; Hrobárik, P.; Hayton, T. W. Use of ^{77}Se and ^{125}Te NMR Spectroscopy to Probe Covalency of the Actinide-Chalcogen Bonding in $[Th(En)\{N(SiMe_3)_2\}_3]^-$ (E = Se, Te; N = 1, 2) and Their Oxo-Uranium(VI) Congeners. *J. Am. Chem. Soc.* **2016**, *138* (3), 814–825.

72. Smiles, D. E.; Wu, G.; Hrobárik, P.; Hayton, T. W. Synthesis, Thermochemistry, Bonding, and ^{13}C NMR Chemical Shift Analysis of a Phosphorano-Stabilized Carbene of Thorium. *Organometallics* **2017**, *36* (23), 4519–4524.

73. Wu, W.; Rehe, D.; Hrobárik, P.; Kornienko, A. Y.; Emge, T. J.; Brennan, J. G. Molecular Thorium Compounds with Dichalcogenide Ligands: Synthesis, Structure, ^{77}Se NMR Study, and Thermolysis. *Inorg. Chem.* **2018**, *57*, 14821–14833.

74. Staun, S. L.; Sergentu, D. C.; Wu, G.; Autschbach, J.; Hayton, T. W. Use of ^{15}N NMR Spectroscopy to Probe Covalency in a Thorium Nitride. *Chem. Sci.* **2019**, *10* (26), 6431–6436.

75. Mullane, K. C.; Hrobárik, P.; Cheisson, T.; Manor, B. C.; Carroll, P. J.; Schelter, E. J. ^{13}C NMR Shifts as an Indicator of U-C Bond Covalency in Uranium(VI) Acetylide Complexes: An Experimental and Computational Study. *Inorg. Chem.* **2019**, *58* (7), 4152–4163.

76. Panetti, G. B.; Sergentu, D. -C.; Gau, M. R.; Carroll, P. J.; Autschbach, J.; Walsh, P. J.; Schelter, E. J. Isolation and characterization of a covalent Ce^{IV}-Aryl complex with an anomalous ^{13}C chemical shift. *Nat. Commun.* **2021**, *12*, 21766-4.

77. Schipper, P. R. T.; Gritsenko, O. V.; Van Gisbergen, S. J. A.; Baerends, E. J. Molecular Calculations of Excitation Energies and (Hyper)Polarizabilities with a Statistical Average of Orbital Model Exchange-Correlation Potentials. *J. Chem. Phys.* **2000**, *112* (3), 1344–1352.

78. Gritsenko, O. V.; Schipper, P. R. T.; Baerends, E. J. Approximation of the Exchange-Correlation Kohn-Sham Potential with a Statistical Average of Different Orbital Model Potentials. *Chem. Phys. Lett.* **1999**, *302* (3–4), 199–207.

79. Du, J.; Seed, J. A.; Berryman, V. E. J.; Kaltsoyannis, N.; Adams, R. W.; Lee, D.; Liddle, S. T. Exceptional uranium(VI)-nitride triple bond covalency from ^{15}N nuclear magnetic resonance spectroscopy and quantum chemical analysis. *Nat. Commun*. **2021**, *12*, 5649.

80. Du, J.; Hurd, J.; Seed, J. A.; Balázs, G.; Scheer, M.; Adams, R. W.; Lee, D.; Liddle, S. T. ^{31}P Nuclear Magnetic Resonance Spectroscopy as a Probe of Thorium–Phosphorus Bond Covalency: Correlating Phosphorus Chemical Shift to Metal–Phosphorus Bond Order. *J. Am. Chem. Soc.* **2023**, *145* (40), 21766–21784.

81. Baker, C. F.; Seed, J. A.; Adams, R. W.; Lee, D.; Liddle, S. T. $^{13}C_{carbene}$ nuclear magnetic resonance chemical shift analysis confirms Ce^{IV}=C double bonding in cerium(IV)–diphosphonioalkylidene complexes. *Chem. Sci.* **2024**, *15* (1), 238–249.

82. Glendening, E. D.; Badenhoop, J. K.; Reed, A. E.; Carpenter, J. E.; Bohmann, J. A.; Morales, C. M.; Landis, C. R.; Weinhold, F. NBO 6.0. Theoretical Chemistry Institute, University of Wisconsin 2013.

83. Bader, R. F. W. *Atoms in Molecules: A Quantum Theory*; Oxford University Press, 1990.

84. Bader, R. F. W. A Bond Path: A Universal Indicator of Bonded Interactions. *J. Phys. Chem. A* **1998**, *102* (37), 7314–7323.

85. Bader, R. F. W.; Slee, T. S.; Cremer, D.; Kraka, E. Description of conjugation and hyperconjugation in terms of electron distributions. *J. Am. Chem. Soc.* **1983**, *105* (15), 5061–5068.

86. Li Manni, G.; Fdez. Galván, I.; Alavi, A.; Aleotti, F.; Aquilante, F.; Autschbach, J.; Avagliano, D.; Baiardi, A.; Bao, J. J.; Battaglia, S.; Birnoschi, L.; Blanco-González, A.; Bokarev, S. I.; Broer, R.; Cacciari, R.; Calio, P. B.; Carlson, R.

K.; Carvalho Couto, R.; Cerdán, L.; Chibotaru, L. F.; Chilton, N. F.; Church, J. R.; Conti, I.; Coriani, S.; Cuéllar-Zuquin, J.; Daoud, R. E.; Dattani, N.; Decleva, P.; de Graaf, C.; Delcey, M. G.; De Vico, L.; Dobrautz, W.; Dong, S. S.; Feng, R.; Ferré, N.; Filatov(Gulak), M.; Gagliardi, L.; Garavelli, M.; González, L.; Guan, Y.; Guo, M.; Hennefarth, M. R.; Hermes, M. R.; Hoyer, C. E.; Huix-Rotllant, M.; Jaiswal, V. K.; Kaiser, A.; Kaliakin, D. S.; Khamesian, M.; King, D. S.; Kochetov, V.; Krośnicki, M.; Kumaar, A. A.; Larsson, E. D.; Lehtola, S.; Lepetit, M.-B.; Lischka, H.; López Ríos, P.; Lundberg, M.; Ma, D.; Mai, S.; Marquetand, P.; Merritt, I. C. D.; Montorsi, F.; Mörchen, M.; Nenov, A.; Nguyen, V. H. A.; Nishimoto, Y.; Oakley, M. S.; Olivucci, M.; Oppel, M.; Padula, D.; Pandharkar, R.; Phun, Q. M.; Plasser, F.; Raggi, G.; Rebolini, E.; Reihe, M.; Rivalta, I.; Roca-Sanjuán, D.; Romig, T.; Safari, A. A.; Sánchez-Mansilla, A.; Sand, A. M.; Schapiro, I.; Scott, T. R.; Segarra-Martí, J.; Segatta, F.; Sergentu, D.-C.; Sharma, P.; Shepard, R.; Shu, Y.; Staab, J. K.; Straatsma, T. P.; Sørensen, L. K.; Cabral Tenorio, B. N.; Truhlar, D. G.; Ungur, L.; Vacher, M.; Veryazov, V.; Voß, T. A.; Weser, O.; Wu, D.; Yang, X.; Yarkony, D.; Zhou, C.; Zobel, J. P.; Lindh, R. The OpenMolcas Web: A Community-Driven Approach to Advancing Computational Chemistry. *J. Chem. Theory Comput.* **2023**, *19* (20), 6933–6991.

87. Sievers, J. Asphericity of 4f-shells in their Hund's rule ground states. *Z. Physik B* **1982**, *45*, 289–296.

88. Rinehart, J. D.; Long, J. R. Exploiting Single-Ion Anisotropy in the Design of f-Element Single-Molecule Magnets. *Chem. Sci.* **2011**, *2* (11), 2078–2085.

89. Bertini, I.; Luchinat, C.; Parigi, G. Magnetic susceptibility in paramagnetic NMR. *Prog. Nucl. Magn. Reson. Spectrosc.* **2002**, *40* (3), 249–273.

90. Gendron, F.; Sharkas, K.; Autschbach, J. Calculating NMR Chemical Shifts for Paramagnetic Metal Complexes from First-Principles. *J. Phys. Chem. Lett.* **2015**, *6* (12), 2183–2188.

91. Godsall, M.; Chilton, N. F. Investigation of the Electronic Structure and Optical Spectra of Uranium (IV), (V), and (VI) Complexes Using Multiconfigurational Methods. *J. Phys. Chem. A* **2022**, *126* (36), 6059–6066.

92. Windorff, C. J.; Evans, W. J. ^{29}Si NMR Spectra of Silicon-Containing Uranium Complexes. *Organometallics* **2014**, *33* (14), 3786–3791.

93. Izod, K.; Liddle, S. T.; Clegg, W. A Convenient Route to Lanthanide Triiodide THF Solvates. Crystal Structures of $LnI_3(THF)_4$ [Ln = Pr] and $LnI_3(THF)_{3.5}$ [Ln = Nd, Gd, Y]. *Inorg. Chem.* **2004**, *43* (1), 214–218.

94. Carmichael, C. D.; Jones, N. A.; Arnold, P. L. Low-Valent Uranium Iodides: Straightforward Solution Syntheses of UI_3 and UI_4 Etherates. *Inorg. Chem.* **2008**, *47* (19), 8577–8579.

95. Kabova, E. A.; Blundell, C. D.; Muryn, C. A.; Whitehead, G. F. S.; Vitorica-Yrezabal, I. J.; Ross, M. J.; Shankland, K. SDPD-SX: Combining a Single Crystal X-Ray Diffraction Setup with Advanced Powder Data Structure Determination for Use in Early Stage Drug Discovery. *CrystEngComm* **2022**, *24*, 4337–4340.

96. *CrysAlis PRO*, Agilent Technologies Ltd. Yarnton, England, 2014.

97. Pawley, G. S. Unit-Cell Refinement from Powder Diffraction Scans. *J. Appl. Crystallogr.* **1981**, *14* (6), 357–361.

98. Coelho, A. A. An Indexing Algorithm Independent of Peak Position Extraction for X-Ray Powder Diffraction Patterns. *J. Appl. Cryst.* **2017**, *50* (5), 1323–1330.

99. Sheldrick, G. M. SHELXT - Integrated Space-Group and Crystal-Structure Determination. *Acta Crystallogr.*, *Sect. A* **2015**, *71*, 3–8.

100. Sheldrick, G. M. Crystal Structure Refinement with SHELXL. *Acta Crystallogr.*, *Sect. C* **2015**, *71*, 3–8.

101. Dolomanov, O. V.; Bourhis, L. J.; Gildea, R. J.; Howard, J. A. K.; Puschmann, H. OLEX2: A Complete Structure Solution, Refinement and Analysis Program. *J. Appl. Cryst.* **2009**, *42* (2), 339–341.

102. Farrugia, L. J. WinGX and ORTEP for Windows: An Update. *J. Appl. Cryst.* **2012**, *45* (4), 849–854.

103. *Persistence of Vision Raytracer*, v.3.7, Persistence of Vision Raytracer Pty. Ltd., 2013.

104. Fung, B. M.; Khitrin, A. K.; Ermolaev, K. An improved broadband decoupling sequence for liquid crystals and solids. *J. Magn. Reson.* **2000**, *142*, 97–101.

105. Bain, G. A.; Berry, J. F. Diamagnetic Corrections and Pascal's Constants. *J. Chem. Ed.* **2008**, *85* (4), 532.

106. Gaussian 16, Revision C.01, Frisch, M. J.; Trucks, G. W.; Schlegel, H. B.; Scuseria, G. E.; Robb, M. A.; Cheeseman, J. R.; Scalmani, G.; Barone, V.; Petersson, G. A.; Nakatsuji, H.; Li, X.; Caricato, M.; Marenich, A. V.; Bloino, J.; Janesko, B. G.; Gomperts, R.; Mennucci, B.; Hratchian, H. P.; Ortiz, J. V.; Izmaylov, A. F.; Sonnenberg, J. L.; Williams-Young, D.; Ding, F.; Lipparini, F.; Egidi, F.; Goings, J.; Peng, B.; Petrone, A.; Henderson, T.; Ranasinghe, D.; Zakrzewski, V. G.; Gao, J.; Rega, N.; Zheng, G.; Liang, W.; Hada, M.; Ehara, M.; Toyota, K.; Fukuda, R.; Hasegawa, J.; Ishida, M.; Nakajima, T.; Honda, Y.; Kitao, O.; Nakai, H.; Vreven, T.; Throssell, K.; Montgomery, J. A., Jr.; Peralta, J. E.; Ogliaro, F.; Bearpark, M. J.; Heyd, J. J.; Brothers, E. N.; Kudin, K. N.; Staroverov, V. N.; Keith, T. A.; Kobayashi, R.; Normand, J.; Raghavachari, K.; Rendell, A. P.; Burant, J. C.; Iyengar, S. S.; Tomasi, J.; Cossi, M.; Millam, J. M.; Klene, M.; Adamo, C.; Cammi, R.; Ochterski, J. W.; Martin, R. L.; Morokuma, K.; Farkas, O.; Foresman, J. B.; Fox, D. J. Gaussian, Inc., Wallingford CT, 2016.

107. Perdew, J. P.; Burke, K.; Ernzerhof, M. Generalized Gradient Approximation Made Simple (PBE0). *Phys. Rev. Lett.* **1996**, *77*, 3865–3868.

108. Cao, X.; Dolg, M. Valence basis sets for relativistic energy-consistent small-core lanthanide pseudopotentials. *J. Chem. Phys.* **2001**, *115* (16), 7348–7355.

109. Cao, X.; Dolg, M. Segmented contraction scheme for small-core lanthanide pseudopotential basis sets. *J. Mol. Struct. THEOCHEM* **2002**, *581* (1-3), 139–147.

110. Dolg, M.; Stoll, H.; Preuss, H. Energy-Adjusted Ab Initio Pseudopotentials for the Rare Earth Elements. *J. Chem. Phys.* **1989**, *90* (3), 1730–1734.

111. Dunning, T. H. J. Gaussian Basis Sets for Use in Correlated Molecular Calculations. I. The Atoms Boron through Neon and Hydrogen. *J. Chem. Phys.* **1989**, *90*, 1007–1023.

112. van Lenthe, E.; Baerends, E. J.; Snijders, J. G. Relativistic Regular Two-component Hamiltonians. *J. Chem. Phys.* **1993**, 99 (6), 4597–4610.

113. van Lenthe, E.; Baerends, E. J.; Snijders, J. G. Relativistic Total Energy Using Regular Approximations. *J. Chem. Phys.* **1994**, *101* (11), 9783–9792.

114. van Lenthe, E.; Baerends, E. J. Optimized Slater-Type Basis Sets for the Elements 1-118. *J. Comput. Chem.* **2003**, *24* (9), 1142–1156.

115. van Lenthe, E.; Ehlers, A.; Baerends, E.-J. Geometry Optimizations in the Zero Order Regular Approximation for Relativistic Effects. *J. Chem. Phys.* **1999**, *110* (18), 8943.

116. Vosko, S. H.; Wilk, L.; Nusair, M. Accurate Spin-Dependent Electron Liquid Correlation Energies for Local Spin Density Calculations: A Critical Analysis. *Can. J. Phys.* **1980**, *58*, 1200–1211.

117. Becke, A. D. Density-Functional Exchange-Energy Approximation with Correct Asymptotic Behavior. *Phys. Rev. A* **1988**, *38* (6), 3098.

118. Perdew, J. P. Density-Functional Approximation for the Correlation Energy of the Inhomogeneous Electron Gas. *Phys. Rev. B* **1986**, *33* (12), 8822.

119. Roos, B. O.; Lindh, R.; Malmqvist, P.-Å.; Veryazov, V.; Widmark, P.-O. New relativistic ANO basis sets for actinide atoms. *Chem. Phys. Lett.* **2005**, *409* (4-6), 295–299.

120. Roos, B. O.; Lindh, R.; Malmqvist, P.-Å.; Veryazov, V.; Widmark, P.-O. New Relativistic ANO Basis Sets for Transition Metal Atoms. *J. Phys. Chem. A* **2005**, *109* (29), 6575–6579.

121. Roos, B. O.; Lindh, R.; Malmqvist, P. Å.; Veryazov, V.; Widmark, P. O. Main Group Atoms and Dimers Studied with a New Relativistic ANO Basis Set. *J. Phys. Chem. A* **2004**, *108* (15), 2851–2858.

122. Chibotaru, L. F.; Ungur, L. Ab Initio Calculation of Anisotropic Magnetic Properties of Complexes. I. Unique Definition of Pseudospin Hamiltonians and Their Derivation. *J. Chem. Phys.* **2012**, *137* (6), 064112.

123. Birnoschi, L.; Chilton, N. F. HYPERION: A New Computational Tool for Relativistic Ab Initio Hyperfine Coupling. *J. Chem. Theory Comput.* **2022**, *18* (8), 4719–4732.

Graphic for Table of Contents and Abstract

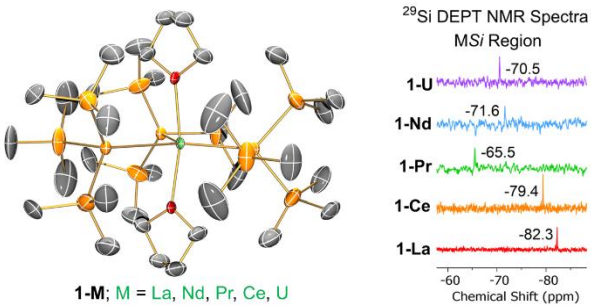

We report an isostructural series of solvated early f-block metal tris-silanide complexes. The high local symmetry of the metal sites gives rich ^{29}Si NMR spectra, allowing us to study paramagnetic shifts of larger nuclei by f-block ions.